

Review

Metal Oxide Chemiresistors: A Structural and Functional Comparison between Nanowires and Nanoparticles

Andrea Ponzoni ^{1,2} 

¹ National Institute of Optics (INO) Unit of Brescia, National Research Council (CNR), 25123 Brescia, Italy; andrea.ponzoni@ino.cnr.it; Tel.: +39-030-3711440

² National Institute of Optics (INO) Unit of Lecco, National Research Council (CNR), 23900 Lecco, Italy

Abstract: Metal oxide nanowires have become popular materials in gas sensing, and more generally in the field of electronic and optoelectronic devices. This is thanks to their unique structural and morphological features, namely their single-crystalline structure, their nano-sized diameter and their highly anisotropic shape, i.e., a large length-to-diameter aspect ratio. About twenty years have passed since the first publication proposing their suitability for gas sensors, and a rapidly increasing number of papers addressing the understanding and the exploitation of these materials in chemosensing have been published. Considering the remarkable progress achieved so far, the present paper aims at reviewing these results, emphasizing the comparison with state-of-the-art nanoparticle-based materials. The goal is to highlight, wherever possible, how results may be related to the particular features of one or the other morphology, what is effectively unique to nanowires and what can be obtained by both. Transduction, receptor and utility-factor functions, doping, and the addition of inorganic and organic coatings will be discussed on the basis of the structural and morphological features that have stimulated this field of research since its early stage.

Keywords: metal oxides; nanowires; nanoparticles; chemiresistors; self-heating; surface functionalization; surface termination



Citation: Ponzoni, A. Metal Oxide Chemiresistors: A Structural and Functional Comparison between Nanowires and Nanoparticles. *Sensors* **2022**, *22*, 3351. <https://doi.org/10.3390/s22093351>

Academic Editor: Antonietta Taurino

Received: 16 March 2022

Accepted: 25 April 2022

Published: 27 April 2022

Publisher's Note: MDPI stays neutral with regard to jurisdictional claims in published maps and institutional affiliations.



Copyright: © 2022 by the author. Licensee MDPI, Basel, Switzerland. This article is an open access article distributed under the terms and conditions of the Creative Commons Attribution (CC BY) license (<https://creativecommons.org/licenses/by/4.0/>).

1. Introduction

Metal oxide nanowires have become a popular class of nanostructures for the development of electronic and optoelectronic devices. Their single-crystalline structure free from extended defects, together with their nm-sized cross section and μm -sized length, make them optimal candidates to merge the potentialities of the nanoscale with efficient electrical transport over much longer distances, with no constrictions from grain boundaries, which typically affect films composed by nanostructures with spherical shapes. In 2001, a fundamental milestone for the technological exploitation of nanowires was reached with the development of a cheap method suitable to synthesize metal oxide nanowires in large amounts and with controlled length, cross-section shape and size [1]. About one year later, these materials were exploited for the first time to develop chemiresistors based on a disordered network of SnO_2 nanowires [2].

These papers inspired intense research in the field of gas sensors, and more generally, in the areas of electronics and optoelectronics. The field has rapidly grown and a broad range of papers have been published about all the relevant aspects of this technological branch. Dedicated reviews have been and are still being regularly published to track the progress in the synthesis of these nanostructures [3–5], their effective integration into functional substrates and devices [6–8] and their exploitation in different applicative fields [9–11].

This witnesses the potentialities and the appeal of these materials for science and technology in a broad sense, and specifically for chemosensing. About 20 years after the aforementioned pioneering papers, the present work aims at reviewing the state of the art of nanowire-based chemiresistors, emphasizing the comparison with nanoparticles. These

are the traditional materials employed in the field but are also the target of recent research. In particular, the manuscript will continue with a section dedicated to the structural and morphological features of nanowires and nanoparticles, from which their potentialities and suitability for technological solutions stem. Synthesis methods will also briefly be reviewed. Gas-sensing models will then be introduced, starting from the knowledge developed with nanoparticles and showing how these concepts have been extended to properly account for shape effects. Finally, some relevant experimental results will be reported to highlight how ideas initially developed for nanoparticles have been further developed to work with nanowires and to discuss those solutions that are unique either to nanoparticles or nanowires.

2. Nanowires: Structure, Synthesis and Gas-Sensor Configurations

This paragraph will briefly overview the structural and morphological features of nanowires, highlighting the differences with respect to nanoparticles. Synthesis methods to prepare single-crystalline nanowires and chemiresistor layouts adopted to exploit these nanostructures will also be resumed. Electrical transport across the circuit elements of chemiresistors based on metal oxide (MOX) nanostructures will finally be introduced in this section. Their dependence from the elementary crystallites will be discussed as the basis for gas-sensing models, and results summarized in Sections 3 and 4, respectively.

2.1. Structural and Morphological Features of Nanowires

The high crystalline quality and the well-defined morphology of nanowires has been widely reported in the literature, particularly by means of electron microscopy techniques, emphasizing the novelty of these features with respect to traditional nanoparticles. An overview of the morphological features of nanowires is reported in Figure 1a–c; images of nanoparticles are reported for comparison in Figure 1d,e. The large length-to-diameter aspect ratio, the absence of grain boundaries through the whole length of the wire, and the well-defined surface termination are the main differences with respect to nanoparticles and nanoparticle assemblies. Nanowires used in gas sensing are typically a few μm or tens of μm long; their cross section has a well-defined polygonal shape, typically a rectangle, a square or a hexagon, with a size of the order of a few tens of nm. The axis of the wire corresponds to a crystalline direction; the exposed surfaces correspond to crystalline planes and are often found to feature an almost atomically flat termination. In addition to nanowires, terms such as nanobelts, nanorods are also used to refer to elongated, single-crystalline nanostructures. A nanobelt is typically used for crystallites with a rectangular cross section, such as those shown in Figure 1; nanowire is used in case of a nearly squared cross section; while nanorod is used for single crystals with a smaller length-to-diameter aspect ratio, though much larger than unity. Nanocubes and nanoprisms will also be considered in this review; these are interesting as links between the ideal nanoparticle and nanowire morphologies. Indeed, nanocubes and nanoprisms feature an almost isotropic shape, typical of nanoparticles, together with faceted surfaces, typical of nanowires.

Before to conclude this section, it is worth mentioning that the name nanowire, or porous nanowire, is sometimes used in the literature to indicate elongated structures composed by assemblies of elementary spherical nanoparticles. In the present work, these nanostructures will not be considered in the family of nanowires; this is because they lack a single-crystalline nature, and concerning electrical properties, their electrical transport within each individual assembly is affected by grain boundaries. Owing to these characteristics, they will be regarded as members of another family of materials, namely the hierarchical assemblies, and will be used for comparison with single-crystalline nanowires.

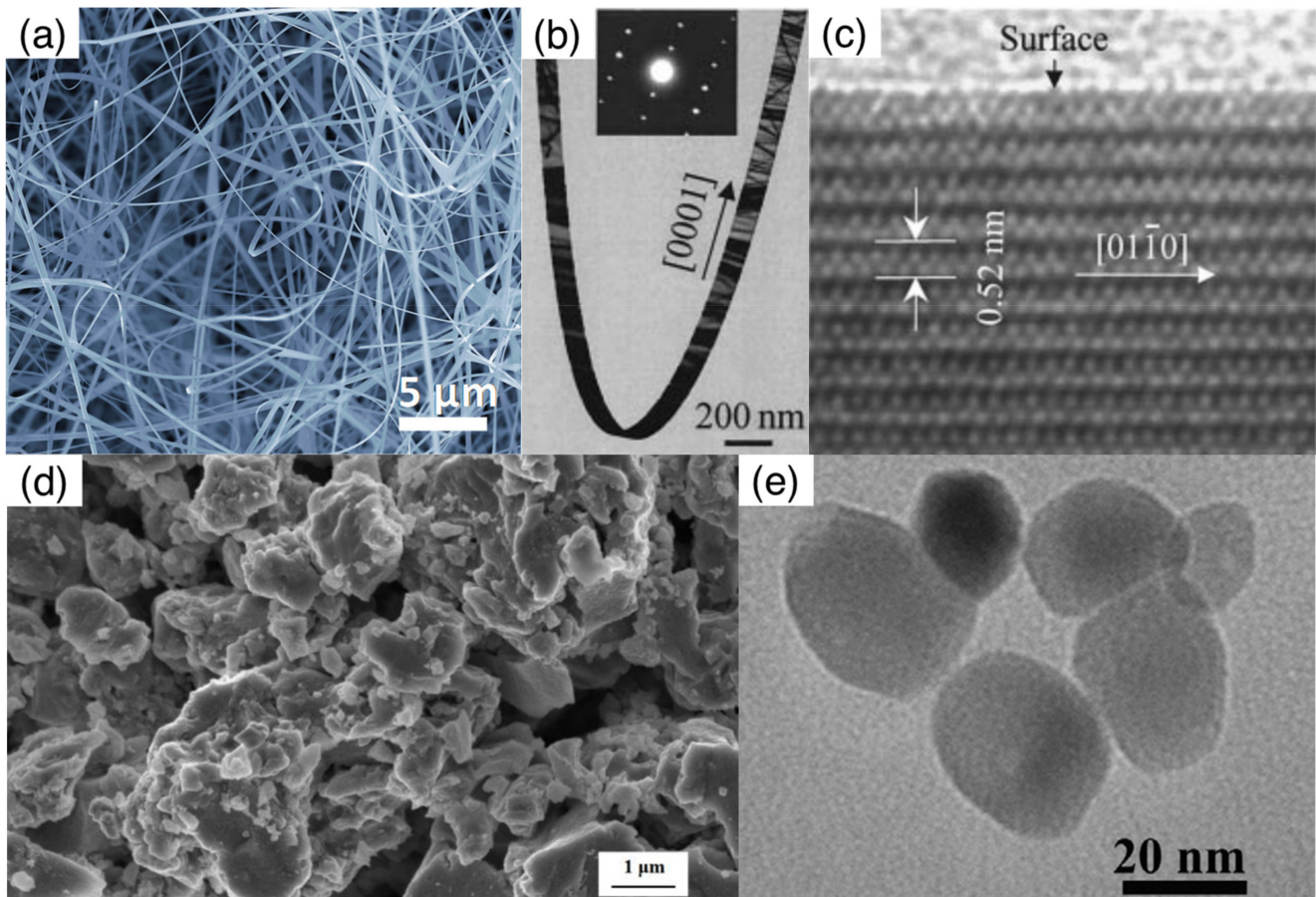


Figure 1. Comparison between the morphological features of nanowires and nanoparticles: (a) Scanning electron microscopy (SEM) picture of SnO₂ nanowires/nanobelts; (b) transmission electron microscopy (TEM) image of a single ZnO nanobelt, the inset reports the selected area electron diffraction (SAED) pattern of the nanobelt; (c) high-resolution TEM (HR-TEM) image of the surface of a ZnO nanowire; (d) SEM image of a network of SnO₂ nanoparticles; (e) TEM image of a few In₂O₃ nanoparticles. Figure 1a is reprinted from [12]. Figure 1b,c are from [1], reprinted with permission from AAAS. Figure 1d is reprinted from [13]. Figure 1e is reprinted from [14], Copyright (2016), with permission from Elsevier.

2.2. Synthesis of Metal Oxide Nanowires

The first paper about nanowire chemiresistors employed a disordered network of SnO₂ nanowires synthesized through the vapor–solid (VS) mechanism [2]. The setup was based on a tubular furnace in which a temperature gradient was realized. MOX powders were used as source material and placed in the warmest region of the tube. The vacuum background was of the order of 10 mbar, and the temperature in this region was adjusted to sublime the powders (around 1350 °C). An Ar flow was used to transport vapors toward the colder region where condensation over substrates occurred [1].

A similar setup has also been widely used for the synthesis through the vapor–liquid–solid (VLS) mechanism. In this case, the substrate is precoated by metallic nanoparticles that catalyze the growth of the nanowire structures. The growth of the oxide nanowire arises from the formation of a eutectic alloy between the metal and the vapor species. As a consequence of the continuous fed of vapors, the alloy reaches a supersaturation condition and the MOX nanowire grows below the alloy nanoparticle [1]. A schematic representation of the VLS mechanism is provided in Figure 2a. The choice of the catalytic nanoparticles, their size and density over the substrate are useful parameters to control the diameter, distribution and density of nanowires [15,16].

Chemical vapor deposition (CVD) techniques have been developed to synthesize nanowires via VS and VLS mechanisms [17–19]. With respect to the aforementioned physical methods, CVD techniques allow for the reduction of the synthesis temperature since they do not require the sublimation of the source powders.

To match the requirements of different device layouts, techniques for deposition over selected areas have been further developed. These include lift-off processes employing high-temperature resists [20], the patterning of the catalyst (for VLS growth) [21] or of the substrate roughness (for VS. growth) [22]. In some papers, the electrodes of the gas-sensor device have been used as catalysts to selectively promote the growth of the nanowires directly from the electrodes [18].

An additional effective method for the patterned growth of nanowires is thermal oxidation. In this case, a metallic film is initially deposited over the desired regions and it is further oxidized at high temperature in an oxidative atmosphere to induce the growth of wire-shaped nanostructures [23,24]. It is worth mentioning that the process often starts with the formation of a polycrystalline oxide layer from the metallic film. This polycrystalline layer is typically composed by rounded grains and nanowires grow out from this layer in a second time, as the oxidation process continues. In principle, a residual polycrystalline film may remain beneath the nanowires, resulting in a device whose properties are given by both morphologies. A similar situation may also occur with nanowires grown by VS and VLS mechanisms directly over the sensor substrate. Indeed, if the synthesis is not properly controlled, spurious depositions may occur, and in the worst cases, a continuous polycrystalline layer may deposit under the nanowire mat. In turn, the undesired film may introduce a non-negligible contribution to the final electrical and sensing properties of the device. In these situations, electron microscopy investigation of gently scratched areas and imaging of cross-section samples are useful methods employed to assess whether the electrical and gas-sensing properties of the device are dominated by nanowires or nanoparticles [20,25]. An example is shown in Figure 2b. In this specific case, the nanoparticles underlying the nanowire network were disconnected one another and they were reasonably supposed to not contribute to the electrical and sensing properties of the device [25].

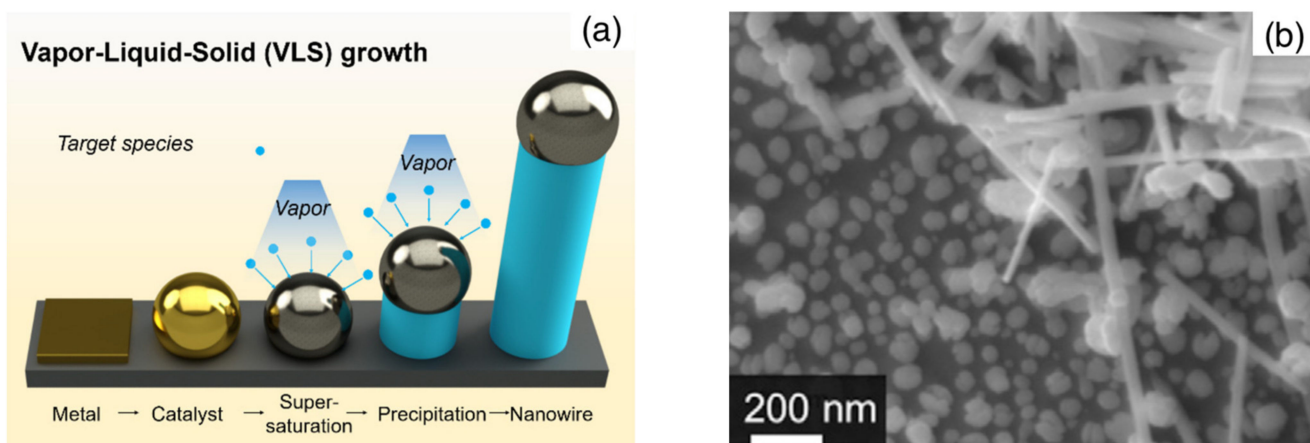


Figure 2. (a) Schematic representation of the vapor–liquid–solid (VLS) growth mechanism employed in the preparation of single-crystalline nanowires; (b) SEM image showing the residual nanoparticles underlying a network of WO_3 nanorods synthesized by oxidation of a polycrystalline film. In this case, nanoparticles are disconnected and are not expected to contribute to the electrical and sensing properties of the macroscopic layer. Figure 2a is from [26]; Figure 2b is reprinted from [25], Copyright (2011), with permission from Elsevier.

Wet chemistry techniques, such as, for example, hydrothermal and sol-gel methods, have also been developed to prepare nanowires. These are appealing approaches owing to their reduced cost, low synthesis temperature and the possibility to finely control the

nanowire properties, including the addition of dopants, by properly selecting the basic chemicals and tuning the solution composition [27,28]. Gas sensors are typically realized by collecting the nanowires from the synthesis apparatus, dispersing them into a solution or a paste that is further directly applied over the sensor substrate [29,30] or used as ink for screen printing [31]. In some cases, MOX nanoparticles have been used as seed crystals to promote the selective growth of nanowires directly over the desired areas of the sensor substrate [32,33].

2.3. Nanowire-Based Chemiresistors: Device Configurations

The simplest way to exploit nanowires in chemiresistor devices is by dispersing a disordered ensemble of these nanostructures over a substrate already provided with electrodes and the heating element. A schematic representation of such a kind of device is shown in Figure 3a together with the main components of its equivalent electrical circuit. Identifying the role of these components in the electrical transport of the device is fundamental to understand its sensing properties, which may be regarded as a gas-induced perturbation to the transport properties of the device. In the equivalent circuit, three main components can be found: nanowires, nanowire–nanowire junctions and the nanowire–electrode contacts, each represented by its equivalent resistor, namely R_{nw} , R_j and R_c [34].

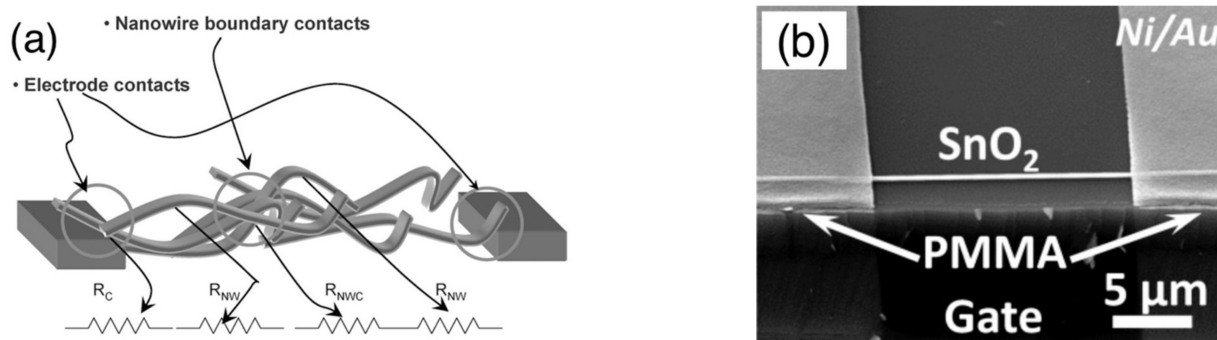


Figure 3. Types of nanowire-based chemiresistors: (a) Schematic representation of a chemiresistor based on a disordered network of nanowires and the main components of the equivalent electrical circuit; (b) SEM image of a chemiresistor based on a single nanowire contacted by two electrodes. Figure 3a is reprinted from [34], Copyright (2010), with permission from Elsevier. Figure 3b is from [12].

In principle, these three elements are the same as in chemiresistors based on nanoparticles; nonetheless, the different morphological features of spherical and wire-shaped nanostructures introduce differences in the relative weight of these equivalent resistors. Indeed, for nanoparticles, it is widely reported that junctions dominate over crystallites, $R_j \gg R_{np}$, where R_{np} is the resistance of nanoparticles and R_j is more often named the grain-boundary resistance. Similarly, considering the large number of grain boundaries in nanoparticle layers, it is often found that $R_j \gg R_c$. As a result, at least in a first approximation, grain boundaries are usually regarded as the dominant elements in nanoparticle-based devices [35,36].

As far as wire-shaped crystallites are considered, there is a large amount of experimental and computational evidence that electrical transport may be no more junction-dominated and crystallites may play a non-negligible role [37–40]. As will be discussed in Section 3, this opens the interesting prospective for the exploitation of the sensing properties of the nanowire body, in addition to nanowire–nanowire junctions. Moreover, considering the reduced number of junctions in the network with respect to the nanoparticle networks, the condition $R_j \gg R_c$ may be no more valid. This will be particularly important in the case of non-Ohmic electrode–semiconductor contacts. In this situation, the reversely biased

contact may feature a contact resistance, R_{cr} , that may be comparable with or even larger than R_j and R_{nw} [19]. The role of electrodes in metal oxide chemiresistors has been recently reviewed based on results achieved with thin-film and thick-film technologies [41]. It provides a complete overview of the different conduction regimes that may take place at the metal–semiconductor interface and the related equations, which are also valid in the case of nanowires.

Another important configuration exploited with nanowire materials is the chemiresistor based on a single nanowire, in which the two electrodes are directly connected through the metal oxide nanowire. A schematic representation of this kind of device is shown in Figure 3. This class of devices is very appealing for both fundamental studies and applications, which will be discussed in the next paragraphs.

Before addressing these arguments, it is worth briefly discussing the electrical circuit of the single-nanowire device. The absence of nanowire–nanowire junctions and the high crystalline quality of the nanowire ease the electrical transport through the semiconducting material. This means that the value of R_{nw} may become comparable with, if not lower than, R_{cr} [42]. To decouple R_{nw} from R_{cr} , the electrical characterization is often carried out using the four-probe configuration instead of the two-probe one [19,43]. As an example, $R_{nw} \approx 76 \text{ M}\Omega$ and $R_{cr} \approx 200 \text{ M}\Omega$ (for an applied voltage of 1 v) were measured at room temperature with a device based on a single SnO_2 nanowire. The wire had a diameter of 50 nm and was placed orthogonally between two parallel Pt electrodes spaced by about 5 μm [19].

3. Gas-Sensing Mechanism

A chemiresistor is a gas sensor based on a sensitive layer that undergoes a variation in its electrical properties upon the interaction with gaseous molecules. The basic concepts underlying the working mechanism of these devices were mainly developed working with thick-film materials and have later been extended to properly account for the nanowire morphology.

The sensing mechanism is usually schematized by means of two functions: the receptor function, which recognizes a chemical substance at the surface of the semiconducting MOX; and the transducer function, which transduces the chemical reactions at the semiconductor surface into the electric output signal [44]. The utility factor, namely the effectiveness of the layer in allowing a proper diffusion of gas through the layer itself, has also been considered in more recent years [45].

These three concepts will be separately introduced in Sections 3.1–3.3 as the basis of the framework underlying the scientific and technological solutions explored in the literature of nanowire-based chemiresistors.

3.1. Receptor Function

Red-ox reactions occurring between the gas molecules and the MOX layer represent the widest-acknowledged phenomena underlying the receptor function of MOX materials.

In these interactions, a key role is played by oxygen ions populating the surface of any metal oxide exposed to ambient air.

At low temperatures (below 150 °C), oxygen is mainly adsorbed molecularly, either in its neutral physisorbed form (O_2), or in its ionic chemisorbed form (O_2^-). Further increasing the temperature, the population of oxygen species becomes dominated by chemisorbed ions in their atomic forms, namely O^- or O^{2-} , the latter dominating above 400–450 °C [35].

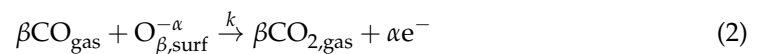
With the aim to focus on aspects responsible for the modulation of the electrical properties of the oxide material, gas-sensing papers typically adopt the following scheme to describe the chemisorption process [35]:



where $O_{2,gas}$ is the molecular oxygen adsorbed from the gas phase; e^- is the elementary electrical charge withdrawn for the MOX conduction band; $O_{\beta,surf}^{-\alpha}$ is the ionic species chemisorbed over the oxide surface; β assumes the values of 1 or 2 for the molecular and atomic forms, respectively; while α is 1 or 2 for singularly and double-ionized ions.

Though Equation (1) provides an oversimplified view of the chemisorption process, it clearly shows the capability of the oxygen chemisorption process to modulate the electrical properties of the MOX semiconductor by modulating its density of charge carriers.

This mechanism is further exploited to detect molecules other than oxygen. Indeed, chemisorbed oxygen ions work as active species promoting the oxidation of other gas molecules (and the reduction of the oxide surface). For example, using carbon monoxide (CO) as prototypical molecule, its interaction with metal oxide gas sensors is typically described according to Equation (2) [35]:



where CO_{gas} is the CO molecule in the gas phase that adsorbs over the oxide surface; $O_{\beta,surf}^{-\alpha}$, e^- , α and β are as above; $CO_{2,gas}$ is the carbon dioxide molecule released back in air after the interaction between CO and the oxide semiconductor; and k is the reaction constant. However, despite its oversimplification, Equation (2) shows how the oxidation of the adsorbed CO molecule causes electrons previously withdrawn by oxygen chemisorption to be released back in the conduction band of the semiconductor.

As far as gases other than CO and O_2 are concerned, reducing gases, such as, for example, ethanol and acetone, are oxidized by the interaction with chemisorbed oxygen following a reaction similar to the one reported in Equation (2) [46]. Oxidizing compounds, such as ozone and nitrogen dioxide, will oxidize the metal oxide surface through a reaction similar to Equation (1) [47].

The receptor function may feature gas specificity; hence, it is useful to address selectivity.

3.2. Transducer Function

As discussed in Section 2.3, the electrical transport thorough the sensitive layer can be decomposed into two contributions: one arising from elementary nanostructures and one from nanostructure–nanostructure junctions.

At microscopic level, junctions are characterized by an energy barrier that hinders the transport of charge carriers. In the case of nanoparticles, this barrier makes the junction conductance much lower than the particle conductance. As a consequence, the macroscopic resistance of traditional gas sensors based on nanoparticle networks, the so-called thick films, features junction-type characteristics, i.e., it is barrier-limited as described by Equation (3) [48]:

$$R \approx R_j = R_0 \exp\left(\frac{E_b}{k_B T}\right) \quad (3)$$

where R_0 is a pre-exponential factor with the dimension of a resistance, which also includes the geometrical details of the effective cross-sectional area for the thick film and its effective length; and E_b is the macroscopic energy barrier characterizing the system.

Until microscopic junctions can be considered almost equal to one another, E_b coincides with the barrier developed at individual microscopic junctions. If not, a statistical picture linking the microscopic and the macroscopic expressions of E_b should be used [49].

A schematic representation of the thick-film chemiresistor and the barrier arising at the nanoparticle–nanoparticle junction is provided in Figure 4. The sensing mechanism of thick films is typically explained in the literature on the basis of this scheme, Equation (3), and relating E_b to the chemisorption and red-ox reactions described by Equations (1) and (2).

The chemisorption of oxygen over the MOX material creates acceptor-surface states, which in turn capture electrons from the semiconductor conduction band. As a consequence,

charges accumulate at the particle–particle interface, developing an electric field that repels electrons from this region.

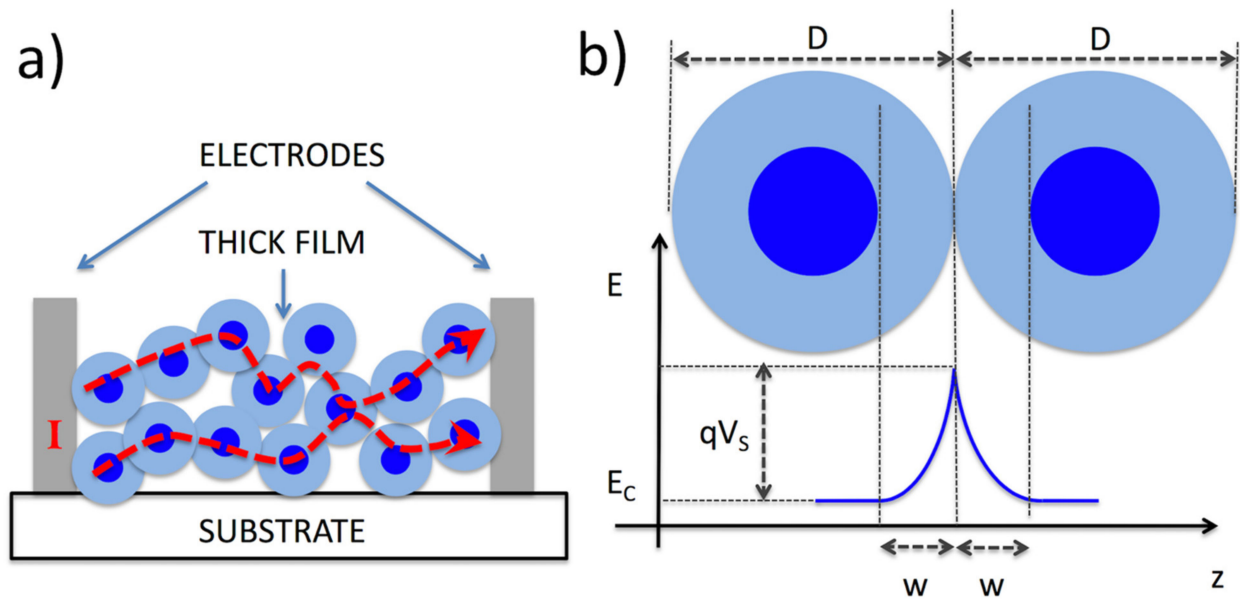


Figure 4. Schematic representation of the sensing mechanism of a thick-film-based gas sensor. The thick-film layout, composed by a network of interconnected particles (a) and the barrier E_b arising at the particle–particle junction (b). In each particle, the surface region depleted from charge carriers is distinguished by light-blue color from the inner portion (blue color) that maintains its unperturbed charge-carrier density. Figure 4a,b are adapted from [50].

From a mathematical point of view, these effects are usually treated by adopting the following assumptions: (i) surface states capture electrons within a layer of width, W , which remains completely depleted by electrons; (ii) treating the surface of MOX crystallites as a flat plane, the mathematical problem can be solved in one dimension (ignoring the effects of the crystallite shape). Such a flat geometry is a good approximation for large grains, i.e., for grains with a diameter much larger than the depletion layer, $D \gg W$. In this case (other situations will be considered in Section 3.4), in the inner part of the grain (up to W) the density of charge carriers is constant and equal to the bulk value of the semiconductor, N_0 . As detailed in Ref. [35], this abrupt distribution of carriers implies a parabolic bending of the semiconductor band structure, with the surface barrier reaching its maximum value E_b at the particle surface and restoring the unperturbed semiconductor properties in the core portion of the particle (between W and the center of the particle). The relationship between E_b and W is given by Equation (4), while the relationship between E_b and the density of surface sites N_S created by oxygen chemisorption is provided by Equation (5):

$$E_b = \frac{q^2 N_0}{2\epsilon} W^2 = \frac{k_B T}{2} \frac{W^2}{\lambda_D^2} \quad (4)$$

$$E_b = \frac{q^2 N_S^2}{2\epsilon N_0} \quad (5)$$

Here, q is the electron charge and ϵ is the dielectric constant of the semiconductor, $\lambda_D = \sqrt{\epsilon k_B T / q^2 N_0}$ is the Debye length, which is a characteristic length of the semiconductor expressing the distance over which mobile charge carriers screen a charge-induced perturbation. Its usefulness will be further discussed in Sections 3.4 and 3.5, dedicated to size- and shape-effects.

A schematic representation of the depletion layer and the band bending is reported in Figure 4b.

Equation (3) combined with Equation (5) shows that the macroscopic resistance of the metal oxide layer depends exponentially from the squared density of surface states, whose value is modulated by the red-ox reactions with gaseous molecules. This relationship explains the high sensing capability of MOX chemiresistors and links this capability to the features of microscopic grain boundaries. The intensity of the sensing response, hereafter shortened as S , is also dominated by grain boundaries. S is calculated as the ratio between the resistances during exposure to the air background and air background with a given diluted amount of the target gas. For an n-type MOX exposed to reducing gases, S is expressed by Equation (6):

$$S = \frac{R_{\text{air}}}{R_{\text{gas}}} \approx \frac{R_{j,\text{air}}}{R_{j,\text{gas}}} = \exp\left(\frac{W_{\text{air}}^2 - W_{\text{gas}}^2}{2\lambda_D^2}\right) = \exp\left(\frac{E_{b,\text{air}} - E_{b,\text{gas}}}{k_B T}\right) \quad (6)$$

Following the convention often adopted in gas sensing [51], which calculates the response in such a way that $S > 1$ during gas exposure, for n-type semiconductors exposed to oxidizing gases it is $S = R_{\text{gas}}/R_{\text{air}}$, while for p-type materials it is the opposite, i.e., $S = R_{\text{gas}}/R_{\text{air}}$ for reducing compounds and $S = R_{\text{air}}/R_{\text{gas}}$ for oxidizing ones.

As discussed in Section 2.3, the resistance of elementary nanowires R_{nw} may play a significant role both in single-nanowire and nanowire-mat-based devices. R_{nw} further depends on the interaction with gases and its relationship with the depletion layer developed at the nanowire surface can be retrieved based on geometrical considerations (conduction takes place only in the inner portion of the wire that is not depleted) [52]. This relationship is here reported in Equation (7) and it is the equivalent of Equation (3) for the nanowire body:

$$R_{\text{nw}} = \frac{1}{q\mu N_0} \frac{L_{\text{nw}}}{\pi\left(\frac{D}{2} - W\right)^2} = \frac{1}{q\mu N_0} \frac{L_{\text{nw}}}{\pi\left(\frac{D}{2} - 2\sqrt{\frac{\varepsilon E_b}{q^2 N_0}}\right)^2} \quad (7)$$

L_{nw} is the nanowire length and μ is the bulk mobility of the metal oxide material.

Nanowire–nanowire junctions are typically modeled as grain boundaries of thick film materials, i.e., using Equation (3). For the nanowire body and the nanowire–nanowire junctions, E_b depends on surface states and the depletion layer, as described by Equations (4) and (5).

For an n-type MOX exposed to a reducing gas, the sensing response of the nanowire body then becomes:

$$S = \frac{R_{\text{nw,air}}}{R_{\text{nw,gas}}} = \frac{\left(\frac{D}{2} - W_{\text{gas}}\right)^2}{\left(\frac{D}{2} - W_{\text{air}}\right)^2} = \frac{\left(\frac{D}{2} - 2\sqrt{\frac{\varepsilon E_{b,\text{gas}}}{q^2 N_0}}\right)^2}{\left(\frac{D}{2} - 2\sqrt{\frac{\varepsilon E_{b,\text{air}}}{q^2 N_0}}\right)^2} \quad (8)$$

3.3. Utility Factor

With reference to Equation (2), an efficient receptor function implies a large k , which in turn means a large consumption of the target gas. If the sensing layer is thick, only the outermost portion of the sensitive film is exposed to the nominal concentration of the target gas, whose amount rapidly decreases proceeding toward the substrate.

These phenomena have been mathematically analyzed in terms of diffusion and surface reaction rates, obtaining the following expression for the gas concentration profile C as a function of the layer thickness, z [53]:

$$C(z) = C_0 \frac{\cosh((L - z)\sqrt{k/D_k})}{\cosh(L\sqrt{k/D_k})} \quad (9)$$

In Equation (9), L is the thickness of the sensitive film; C_0 is the gas concentration in air and at the outermost layer of the sensitive film; and $C_0 = C(z = 0)$, $D_k = \frac{4r_p}{3} \sqrt{\frac{2RT}{\pi M}}$ is the Knudsen diffusion coefficient, which depends on the pore radius r_p , the molecular mass M , the working temperature T and the gas constant R .

This has been a leading concept in the development of several sensing layers and its optimization was identified as one of the key factors in some very remarkable achievements. Some examples will be discussed in Section 4.

3.4. Size Effects

The beneficial effects arising from a reduced diameter of elementary nanostructures is among the widest-acknowledged results in gas sensing. It has been widely reported in experimental works [44,54], and theoretical papers have explained its relationship with the optimization of the transducer function at the level of individual nanostructures [55–57].

Depending on the ratio between W and the diameter D of the elementary nanostructure, the electrical and sensing properties enter in different regimes. Among these, only the extreme cases admit an analytical solution, namely (i) $D \gg W$ and (ii) $D \leq \lambda_D$ (which also means $D < W$, according to Equation (4)). The intermediate conditions need numerical solutions [57].

In the first case, as evident from Equations (4) and (5) and from Figure 4, the interaction with gases alters the electrical properties of a given metal oxide only within a surface layer of thickness W . In the region beyond W , the properties of the material are insensitive to interaction with gases.

If the diameter of the nanostructure is further reduced below the extent of W , till the size of λ_D , the material enters into the second regime, in which grains are fully depleted from electrons (apart those that are thermally promoted into the conduction band). In this condition, the barrier height at junctions is lower than the thermal energy (flat band condition). Phenomena described in Section 3.1 modulate the conductance of the semiconductor by modulating the position of its Fermi level, and the resulting transducer function is even more efficient than the one described by Equations (4) and (5). In particular, being $D < W$, D becomes the relevant characteristic length in the response intensity. More specifically, the response S increases with $D^{-1/2}$ and with D^{-1} for reducing and oxidizing gases, respectively. The complete mathematical description of these regimes can be found in dedicated papers [55,56].

3.5. Shape Effects

Equation (4) is valid for plate-shaped crystallites or for other shapes in the case of large grains ($D \gg \lambda_D$), so that the surface of the crystallite can be considered almost flat. If grains are not large, as is often the case in nanostructures, shape effects apply to the $E_b = E_b(W)$ relationship modifying it with respect to Equation (4). As already introduced in Section 3.4, only a few regimes can be solved analytically, and this also holds for shape effects [57,58]. Despite such intrinsic difficulties, the proposed models and simulations agree that the spherical shape is the most effective to enhance the transduction mechanism [55,56,58]. In this sense, it is useful to compare two crystallites having the same diameter and electronic properties, undergoing the same interactions with gases, in particular oxygen, but featuring a spherical and cylindrical shape, respectively. Theories predict that the depletion layer is larger in the spherical crystallite than in the cylindrical one and that the former enters in the full-depletion regime earlier (for lower oxygen concentrations in the atmosphere) than the latter [55,56,58].

Moreover, spatially-resolved scanning tunneling spectroscopy (STS) experiments have shown that oxygen adsorption occurs preferably at grain boundaries and to a lesser extent over the crystallite surface [59]. This will reasonably have important implication in the comparison between nanowires and nanoparticles, since nanowire networks intrinsically feature a much lower density of junctions than thick films composed by nanoparticles. From

this point of view, the spherical shape emerges once again as potentially more effective than the wire shape.

4. Approaches Adopted to Control the Sensing Properties of Gas Sensors

This section reports an overview of different strategies reported in the literature to exploit the morphological and structural features of MOX nanostructures to emphasize and tune their sensing capabilities.

Considering the vastness of the literature about nanowire chemiresistors, a complete overview of the field is out of the scope of the present work. Results will be shown referring mainly to SnO₂, ZnO and WO₃, which have been suitable benchmark materials to compare nanowires and nanoparticles since the early times of nanowire literature.

4.1. Porosity (Utility Factor) and Network Effects

As discussed in Section 3, small grains and large pores are fundamental features to optimize, respectively, the transduction mechanism and the efficiency of gas diffusion through the whole volume of the sensing layer.

Concerning traditional thick films, it has often been observed that these two morphological features may conflict one another, with small nanoparticles often implying small pores [60]. To solve this issue, several authors focused their work on the development of hierarchical nanostructures. These exploit nanoparticles organized in μm -sized assemblies that are further distributed in a disordered network connecting the electrodes [60]. Hollow spheres [61–63], fibers [64–66] and hollow fibers [67,68] are some popular examples.

Nanowire networks, on the other hand, intrinsically offer the possibility to merge these two requirements thanks to their nm-sized diameter and elongated shape, which often result in large voids, allowing an efficient gas diffusion.

Some remarkable results obtained through the optimization of these parameters will be reported in the following part of this section and will be summarized at the end of it in Table 1.

For example, Kida et al. compared the sensing properties of different SnO₂ nanowire networks with varying length-to-diameter aspect ratios, including nanocubes with a size of ≈ 13 nm and nanorods with a diameter and length of ≈ 25 nm and ≈ 500 nm, respectively [69]. These nanostructures revealed excellent sensitivity to both ethanol and H₂, demonstrating a very effective structure for the optimization of the transducer function and the utility factor. Concerning ethanol, a recent review highlighted that the response of these nanorods, $\approx 10^5$ to an ethanol concentration of 100 parts per million (ppm), emerged as the largest response reported in the literature among more than recent 80 papers about chemiresistors based on pure SnO₂. In addition, nanocubes were identified as remarkable outliers in such a review [70]. The situation is similar for H₂: these nanostructures revealed a very high response, at least comparable with state-of-the-art nanostructures such as thick films and hierarchical nanostructures with very thin, fiber-like shapes [71,72]. In addition to the excellent sensitivity in a general sense, the authors observed that size effects are emphasized with small molecules, in particular H₂, while for larger molecules such as ethanol, the nanorods exhibited the best performance despite their diameter being larger than the nanocube size. This was ascribed to diffusion phenomena. For ethanol, this could take place in an effective manner only in the case of nanorods, whose length allowed for a larger porosity. Differently, for H₂, the lower porosity featured by the nanocube layer was sufficient for an efficient diffusion of such a small molecule, thus emphasizing the beneficial size effects of the small nanocubes.

Other remarkable ethanol responses have been reported in the literature exploiting hierarchical assemblies of elementary nanowires. In this sense, it is worth mentioning the work by Firooz et al. that reports the response to 300 ppm of ethanol increasing from 1600 to 4000 when the structure is changed from a disordered network of nanowires to flower-like assemblies of nanowires [73]. These values are competitive with the largest

responses recorded with nanoparticle-based devices, including thick films and hierarchical nanospheres with trimodal porosity [71,74,75].

In addition to the intrinsic porous structure, nanowire networks feature the presence of nanowire–nanowire junctions, which have often been invoked as key elements for the improvement of nanowire-based chemiresistors. This reasonably stems from the more efficient transduction mechanism of junctions with respect to the nanowire body (exponential vs. quadratic response, as depicted in Equations (6) and (8)), and to the preferential adsorption at grain boundaries discussed in Section 3.5. For example, junctions have been proposed to explain the remarkable responses to NO₂ recorded at room temperature with In₂O₃ nanowire networks, in contrast with the much lower responses obtained with chemiresistors exploiting the single-nanowire configuration [76]. In particular, it is worth noting that the mentioned nanowire network revealed the ability to respond to NO₂ concentrations lower than 50 parts per billion (ppb), which is the threshold limit for outdoor applications and is often used as a benchmark for sensing technologies, including thick films and hierarchical nanostructures [77–79]. On the other hand, such outstanding room-temperature sensitivity was obtained, exploiting an almost irreversible interaction with NO₂, which required UV illumination to quickly restore the baseline.

Other remarkable NO₂ responses at the level of 50 ppb and below were achieved, exploiting hierarchical WO₃ nanostructures [80]. In this case, the devices exploited an embedded heater to work at the temperature of 300 °C, which ensured an effective compromise between intense response and acceptable response and recovery times.

Though several papers report the abundance of junctions as beneficial for nanowire chemiresistors [25,76,81,82], some works have recently pointed out the need for controlling the density of the nanowire network to achieve an optimal compromise between the density of junctions and the size of pores, which have opposite dependencies from the network density [83,84].

Table 1. Chemiresistors based on pure (neither doped nor functionalized) metal oxide (MOX) nanoparticles and nanowires. The response intensity S is calculated as $S = R_{\text{gas}}/R_{\text{air}}$ for NO₂ and as $S = R_{\text{air}}/R_{\text{gas}}$ for other compounds at the sensor temperature T . Gas concentrations are expressed in parts per million (ppm) or parts per billion (ppb), and, in the T column, RT stands for ‘room temperature’.

MOX, Morphology	T (°C)	Gas, Concentration	S	Ref.
SnO ₂ , nanowire network	250	Ethanol, 100 ppm	10 ⁵	[69]
SnO ₂ , nanowire network	300	H ₂ , 200 ppm	200	[69]
SnO ₂ , nanocubes network	250	Ethanol, 100 ppm	6000	[69]
SnO ₂ , nanocubes network	300	H ₂ , 200 ppm	270	[69]
SnO ₂ , nanowire network	300	Ethanol, 300 ppm	1600	[73]
SnO ₂ , hierarchical flower-like assemblies of nanowires	275	Ethanol, 300 ppm	4000	[73]
SnO ₂ , thick films	300	Ethanol, 100 ppm	1520	[71]
SnO ₂ , thick films	300	H ₂ , 200 ppm	87	[71]
SnO ₂ , thick films	300	Ethanol, 100 ppm	2400	[74]
SnO ₂ , hierarchical nanospheres of nanoparticles	400	Ethanol, 5 ppm	316	[75]
SnO ₂ , hierarchical fibers of nanoparticles	250	H ₂ , 100 ppm	25	[72]
SnO ₂ , hierarchical fibers of nanoparticles	150	NO ₂ , 125 ppb	90	[78]
WO ₃ , 3D hierarchical assembly of nanowires	300	NO ₂ , 50 ppb	6	[80]
WO ₃ , thick film	300	NO ₂ , 50 ppb	1.5	[77]
WO ₃ , nanolamellae	200	NO ₂ , 200 ppb	70	[79]
In ₂ O ₃ , nanowire network	RT	NO ₂ , 50 ppb	2	[76]

4.2. Surface Termination

As discussed in Section 2.1, the surface termination of nanowires with well-defined crystalline planes is one of its unique features with respect to traditional nanoparticles. Indeed, different facets exhibit different densities of atomic edges, steps and unsaturated coordination sites that are all relevant for the interaction with gases [85,86]. Low-index surfaces of macroscopic SnO₂ single crystals have been widely studied in surface science, showing their different behavior with respect to oxygen chemisorption [85]. Similarly, broad evidence has been collected demonstrating the surface-termination dependence of the interaction between macroscopic TiO₂ single crystals and gaseous molecules [86].

Atomically resolved scanning tunneling microscopy studies have been applied to SnO₂ nanowires pre- and post-surface-oxidation and surface-reduction treatments. Results have shown a similar ordering of surface atoms for these nanocrystals and macroscopic crystals typically studied in traditional surface science, providing an important conceptual link between the two disciplines [87].

More recently, attention has been dedicated to high-index surfaces, which are expected to be more suitable than low-energy ones for gas sensing owing to their richness in atomic edges, steps and unsaturated coordination sites. This has been confirmed both computationally and experimentally. Density functional theory (DFT) calculations confirmed that the exothermic oxygen chemisorption over SnO₂ surfaces is more favorable (larger energy reduction) for high-energy facets such as (221) than for low-energy ones, such as (110) [88–90]. From an experimental point of view, the comparison between the gas sensing properties of low- and high-index surfaces has been realized through the synthesis of nanopolyhedra exposing high-energy facets and the synthesis of elongated nanopolyhedra, laterally bonded by low-energy facets, using SnO₂ as example material [91]. In this way, the control over the length of the elementary nanostructures allowed for tuning of the balance between the areas of high- and low-energy planes, and in turn, their relative contributions to the sensing response. Similar improvements have also been recorded for other oxides, including Fe₂O₃ [92], Cu₂O [90], NiO [30] and TiO₂ [93]. In 2018, these results were analyzed as a whole. It was concluded that in most of cases, facets revealed more effectiveness than surface area in the enhancement of the sensor response in a broad sense, i.e., the improvement was observed toward different gases [94].

In other papers, the surface termination was proposed to explain the observed differences about the partial selectivity exhibited by nanowires and nanoparticles. For example, comparing SnO₂ nanowire and nanoparticle networks, it was observed that none of the two morphologies could be indicated as more sensitive than the other in an absolute way, but these considerations are gas-dependent. As reported in Figure 5, nanowires were found to be more sensitive to compounds such as acetone, dimethyl methylphosphonate (DMMP) and dipropylene glycol monomethyl ether (DPGME), while nanoparticles were more sensitive to CO and NH₃ [95]. Similar results were also obtained with In₂O₃ nanowires and nanoparticles [95]. Differences were also observed in the case of WO₃, for which nanoparticles and nanorods exhibited similar responses to ammonia; while in the case of ethanol and acetone, the response of nanoparticles was about one order of magnitude larger than the response of nanorods [25].

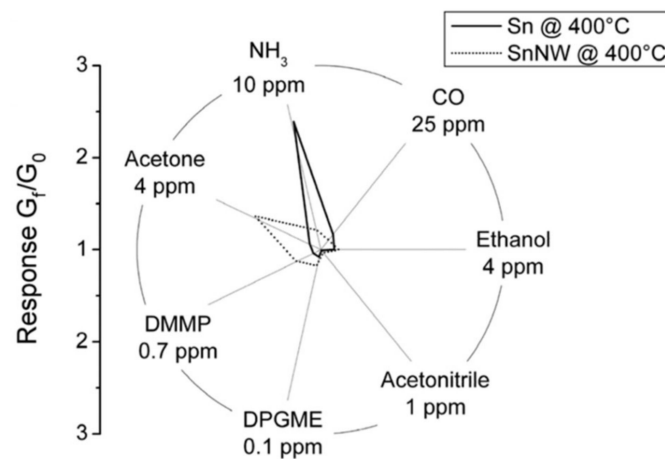


Figure 5. Surface termination effects in nanowire- and nanoparticle-based chemiresistors. Polar plot comparing the response of SnO₂ nanowires (SnNW) and nanoparticles (Sn) against different chemicals. © 2008 IEEE. Reprinted, with permission, from [95].

4.3. Doped Nanostructures

In this paper, the term ‘doping’ will be intended according to its meaning from the field of semiconductors, in which a dopant is an additive element introduced in the lattice of the host material as an interstitial or substitutional atom/ion [96]. Those cases in which the additive element is deposited in the form of cluster over the supporting MOX are referred to as surface functionalization and will be treated in Section 4.4.

In the field of thin- and thick-film chemiresistors, the dispersion of dopants has been widely used to address several objectives: (i) to increase the thermal stability of the film micro/nanostructure by hindering grain-coarsening phenomena; (ii) to decrease the electrical resistivity of the film; (iii) to control its Debye length and the space-charge-layer depth; (iv) to tailor the response and the partial selectivity of a given material according to specific requirements.

Between these objectives, the former is probably the most shape-dependent. For thin and thick films composed by more or less compact aggregates of spherical nanostructures, grain coarsening was recognized as an important limiting factor for the long-time stability of MOX-based chemiresistors [97]. Electron microscopy investigations revealed that these phenomena occur at grain boundaries and involve the rearrangement of atom ordering at these interfaces. Reordering is such that larger grains coarsen by subtracting atoms from smaller grains [98]. Considering the importance of the grain size for the sensing properties of MOX, these microscopic phenomena affect the macroscopic properties of the device, such as its baseline and sensing response. To suppress these microstructural drifts, dopants have been widely used in the field of ceramic materials. These additives act as blocking elements for grain-boundary migration and phase transition [97,99].

As for nanowires, their elongated single-crystalline structure has already been proposed as a possible solution for such microstructural drifts in the first publication about nanowire-based gas sensors [2]. This is intrinsic for devices based on a single nanowire or aligned nanowires owing to the total absence of grain boundaries. For nanowire networks, which feature the presence of nanowire–nanowire junctions, an increased stability with respect to nanoparticles was reported after a study lasting about 1 month [100].

From this point of view, Ga₂O₃ is of particular interest. It has been largely studied as polycrystalline-film gas sensor owing to its thermal and chemical stability, which make it an appealing material for gas sensing [101,102]. In its pristine form (not intentionally doped), grains about 20 nm large remain stable at the temperature of 900 °C [103], while for pristine SnO₂ the stable diameter is of the order of 100 nm [104]. Ga₂O₃ nanowires have also been investigated for H₂ and volatile organic-compound sensing [105,106].

In addition to grain coarsening, doping also affects all the other aforementioned features of the device. Doped materials typically exhibit a baseline that is different from that of the pristine host. From this viewpoint, dopants are often used to decrease the baseline of materials that exhibit a large resistivity. Indeed, it may happen to deal with materials/sensors whose baselines approach or even exceed the GOhm [97,107,108]. The electrical signals of these devices are easily read by laboratory equipment but may be hard to read with cheap commercial electronics. Research in readout systems is studying innovative and cheap approaches suitable to read resistances spanning a broad range [109,110]. Nonetheless, avoiding very large values may be an appealing feature for easy and effective device exploitation [111]. Doping of TiO_2 is a typical example: In its pure form, titania features the presence of oxygen vacancies but its resistivity remains quite large, and dopants such as Nb are often used to mitigate this drawback owing to the donor properties of Nb in TiO_2 . Nb-doped TiO_2 has been studied both in the form of thick films [97], nanorods [112] and hierarchical structures such as nanotubes [113]. Ga_2O_3 is also highly resistive at the typical gas-sensing temperatures (below 600°C), and dopants such as, for example, Si and Sn, are often used to increase the charge-carrier density [114,115].

Altering the baseline of the host material through the introduction of dopants also affects the transduction mechanism through the modulation of the Debye length. According to semiconductor theory (see Section 3.1), the increase in charge carriers implies shorter Debye length (and space-charge layer), which in turn implies a reduced sensor response. Generally speaking, a balance between an easy-to-read baseline and an effective Debye length should be considered.

In some cases, doping may also cause the material to switch from n- to p-type or vice-versa. Using TiO_2 as example, this is the case for Cr doping, which enters in the TiO_2 lattice as electron acceptor, hence introducing holes. P-type Cr-doped TiO_2 has been synthesized introducing Cr at the concentration of ca 8% at. [107].

In addition, dopants also affect the receptor function of the host material and can be exploited to tune the partial selectivity of MOX. For example, concerning Ga_2O_3 , Sb doping enhances its response to O_2 , while Na-K co-doping improves its sensitivity to humidity [116,117]. Zn doping in In_2O_3 nanowires was reported to modify the response spectrum of the guest oxide by decreasing its response to NO_2 and increasing the response to reducing gases, more specifically to H_2 , CO, ethanol and acetone [118]. A general increase in the response toward reducing compounds was also observed for Zn-doped In_2O_3 hierarchical nanospheres composed by spherical crystallites, with emphasis on the enhancement of the response to triethylamine [119]. Both for nanowires and other nanostructures, the effect of Zn doping on In_2O_3 -sensing properties is usually ascribed to the formation of point defects, such as Zn interstitials, oxygen and In vacancies in the host matrix [118,120]. In some papers, Zn has also been proposed to stimulate the phase transition of the host oxide. This is the case, for example, of the In_2O_3 transition from body-centered cubic (bcc) to rhombohedral (rh). Introducing Zn in single-phase pristine bcc- In_2O_3 , the material changed into a polycrystalline mixture of bcc/rh, with the portion of the rh phase increasing with the increase in the dopant [120]. This structural modification was accompanied by a morphological evolution from single-crystalline nanocubes to hierarchical polycrystalline nanoflowers. The joint structural and morphological modification implied more point and extended defects, including bcc-rh interfaces, and an increased surface area, which were identified as the key features underlying the increased sensitivity of doped samples to NO_2 . Morphological changes promoted by Zn doping were also observed in hierarchical spheres composed by SnO_2 nanorods, which turned to assemblies of sheet-shaped crystallites. Zn-doped SnO_2 nanostructures revealed more sensitivity in general toward reducing gases, including ethanol, glycol and acetone [121].

4.4. Inorganic Heterostructures

The functionalization of MOX surfaces with inorganic additives is probably the widest-used method to improve and tune the properties of MOX chemosensors. Both metallic

nanoparticles and MOX nanoparticles have been widely investigated as additives to MOX thick films and have also further been applied to MOX nanowires. Over the years, several review papers have been specifically dedicated to this topic. In the past, these were mainly concerned with chemiresistors based on thick and thin films [122], while in more recent years, results obtained with other morphologies such as nanowires, nanosheets and hierarchical structures have also been included [123,124].

4.4.1. Functionalization with Metallic Nanoparticles

As for metallic additives, their effect (often termed sensitization) on gas-sensing properties occurs through two mechanisms: electronic and chemical [125]. The former arises from the different work functions of the metal and the MOX semiconductor (ϕ_m and ϕ_s). It is generally explained starting from the ideal situation of the two isolated materials that are further brought into contact. Referring to an isolated n-type MOX, its Fermi level lies inside the bandgap, close to the conduction band owing to oxygen vacancies. As a result, it is usually observed that $\phi_m > \phi_s$, meaning that it is easier to extract electrons from the semiconductor than from the metal. When the two systems are coupled, the Fermi levels' alignment implies the transfer of electrons from the semiconductor to the metal, resulting in a depletion layer in the MOX side of the interface [35,126]. This effect adds up with the depletion layer induced by oxygen chemisorption described in Section 3 [125]. A schematic representation of the electronic sensitization is shown in Figure 6a. The second mechanism stems from the catalytic properties of nanosized metallic particles, which are able to dissociate molecules into byproducts that are further spilled over the supporting oxide (spill-over effect) facilitating the overall response of the composite material [122]. For chemosensing, the dissociation of molecular oxygen into reactive O^- ions promoted by metals such as Au and Pd is of particular relevance [127–129]. It acts by increasing both the density of chemisorbed oxygen ions and the depletion-layer extension in the surrounding of the metallic nanoparticle, as schematically shown in Figure 6b.

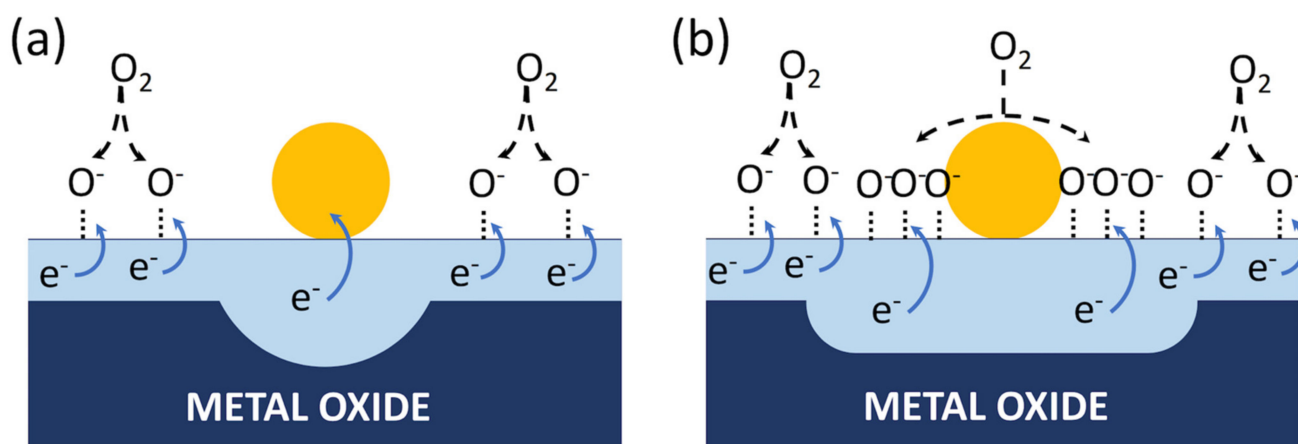


Figure 6. Schematic representation of metal oxide sensitization by means of metallic nanoparticles. (a) Electronic sensitization: the depletion layer is extended at the metal–metal oxide interface as a consequence of Fermi level alignment between the two materials; (b) spillover of oxygen molecules, O_2 , promoted by the metallic nanoparticle: oxygen molecules from the gas phase are dissociated by the metallic nanoparticle and further chemisorbed over the metal oxide surface. In the surrounding of the nanoparticle, this causes both an increase in the density of active ions and an extended depletion region.

In addition to oxygen, other molecules are also directly spilled over by suitable metallic nanoparticles. A widely known example is the spill-over of H_2 molecules promoted by Pd and Pt, which has been largely exploited in thick-film technology [122] as well as with nanowire chemiresistors, both in the single-nanowire [129] and nanowire-network configurations [18,69].

In other papers, the synergy between the intrinsic catalytic activity of metallic nanoparticles and the increased density of reactive oxygen arising from oxygen spillover is proposed as the main reason for the increased response. This is the case of ethanol responses enhanced by Au or Pt nanoparticles. To cite a few examples, Au functionalization was employed with SnO₂ layers, both in the form of thick films [130] and nanowires [131]; Pt was used with SnO₂ hollow spheres [132] and networks of SnO₂ nanorods [133]. The same combination of metal-promoted effects was also proposed to explain the improved response to H₂S observed for several Au-supported MOX, including WO₃ nanorods [134] and nanoparticles [135].

A summary of the numerical responses recorded with these materials, both in their pristine and functionalized form, is reported in Table 2. In addition to the improved response intensity toward the target gas, it is worth mentioning the beneficial effect about the optimal working temperature, which is often lowered by the functionalization with metallic nanoparticles.

In recent years, bimetal nanoparticles composed by alloyed metals have attracted large attention owing to their coupling with the supporting oxide, which is different from the coupling of the respective monometallic components. For example, the AuPd system has been studied by different research groups using different supporting metal oxides. Considering SnO₂ thick films as support, the different balance between oxygen spillover and electronic sensitization has been reported for Au, Pd and AuPd nanoparticles [128]. Despite these insightful results, the effects of the bimetallic functionalization with respect to the functionalization with individual metal is still in an early stage. Different results have been published so far, without reaching a comprehensive, uniform picture of the involved phenomena. For example, enhanced performances have been reported for AuPd-functionalized SnO₂ thick films to a broad range of compounds, including CO, CH₄ and NH₃, [136]. However, other papers reported AuPd functionalization as less effective for CO, ethanol and CH₄ with respect to the pristine and single-metal-functionalized SnO₂ [128]. Morphologies other than thick films have also been considered for this kind of functionalization. Some examples are SnO₂ flower-like hierarchical assemblies of nanosheets, which showed an increased sensitivity to several compounds, including formaldehyde and acetone [137]; SnO₂ hollow spheres, for which the effectiveness of the functionalization was proven against dimethyl disulfide; and WO₃ nanowires, tested against butanol [138].

Before concluding this paragraph, it is worth mentioning another approach to exploit the metal–semiconductor interface for gas sensing, which was proposed by Wei et al. [139] working with a single-nanowire device. In this case, the metallic structure was the electrode, which formed a reverse biased Pt–ZnO junction in the single-nanowire device. Based on the discussion reported in Section 2.3, though such an interface is also present in devices based on MOX thick films and nanowire networks, it is particularly meaningful in the single-nanowire device, for which such a junction may dominate the overall device resistance. In particular, Wei et al. [139] proposed a sensing mechanism based on the modulation of the Schottky barrier E_{ms} at the metal–oxide interface induced by gas adsorption:

$$R \approx R_{cr} + R_{nw} \approx R_{cr} \propto \exp\left(\frac{E_{ms}}{k_B T}\right) \exp\left(-\frac{qV_{cr}}{k_B T}\right) \quad (10)$$

$$S \approx \frac{R_{cr,gas}}{R_{cr,air}} = \exp\left(\frac{E_{ms,gas} - E_{ms,air}}{k_B T}\right) \quad (11)$$

V_{cr} is the voltage drop over the reversely biased metal–oxide interface and other symbols are defined as above. Although in this case the metal is not dispersed in the form of nanoparticles—hence neither the electronic nor the catalytic sensitization are optimized—its transduction mechanism features an exponential dependence from E_{ms} , which is more efficient than the quadratic form of the nanowire body described by Equation (8).

Table 2. Chemiresistors based on metal oxide (MOX) nanostructures functionalized with metallic nanoparticles. The response intensity S is calculated as $S = R_{\text{air}}/R_{\text{gas}}$ at the sensor temperature T . In case of no response at this temperature, ‘no resp.’ is reported in the S column. Gas concentrations are expressed in parts per million (ppm).

Supporting MOX, Morphology	Functionalization	T (°C)	Gas, Concentration	S	Ref.
SnO ₂ , nanowire network	–	250	Ethanol, 100 ppm	10 ⁵	[69]
SnO ₂ , nanowire network	Pd	250	Ethanol, 100 ppm	1.1 × 10 ⁵	[69]
SnO ₂ , nanowire network	–	300	H ₂ , 200 ppm	200	[69]
SnO ₂ , nanowire network	Pd	250	H ₂ , 200 ppm	800	[69]
SnO ₂ , nanocubes network	–	250	Ethanol, 100 ppm	6000	[69]
SnO ₂ , nanocubes network	Pd	250	Ethanol, 100 ppm	6000	[69]
SnO ₂ , nanocubes network	–	300	H ₂ , 200 ppm	270	[69]
SnO ₂ , nanocubes network	Pd	250	H ₂ , 200 ppm	300	[69]
SnO ₂ , nanowire network	–	150	H ₂ , 40 ppm	no resp.	[18]
SnO ₂ , nanowire network	Pd	150	H ₂ , 40 ppm	3	[18]
SnO ₂ , single nanowire	–	100	H ₂ , 1 ppm	no resp.	[129]
SnO ₂ , single nanowire	Pd	100	H ₂ , 1 ppm	5	[129]
SnO ₂ , thick film	–	270	Ethanol, 200 ppm	28	[130]
SnO ₂ , thick film	Au	220	Ethanol, 200 ppm	128	[130]
SnO ₂ , hollow spheres	–	325	Ethanol, 5 ppm	95	[132]
SnO ₂ , hollow spheres	Pt	325	Ethanol, 5 ppm	1400	[132]
SnO ₂ , nanorod network	Pt	300	Ethanol, 200 ppm	40	[133]
WO ₃ , nanorod network	–	350	H ₂ S, 1 ppm	4	[134]
WO ₃ , nanorod network	Au	350	H ₂ S, 1 ppm	100	[134]
WO ₃ , thick film	–	300	H ₂ S, 1 ppm	3	[135]
WO ₃ , thick film	Au	300	H ₂ S, 1 ppm	7	[135]
SnO ₂ , thick film	–	300	CO, 50 ppm	10	[128]
SnO ₂ , thick film	Au	300	CO, 50 ppm	100	[128]
SnO ₂ , thick film	Pd	300	CO, 50 ppm	100	[128]
SnO ₂ , thick film	AuPd	300	CO, 50 ppm	2.5	[128]
SnO ₂ , thick film	–	300	Ethanol, 10 ppm	50	[128]
SnO ₂ , thick film	Au	300	Ethanol, 10 ppm	500	[128]
SnO ₂ , thick film	Pd	300	Ethanol, 10 ppm	150	[128]
SnO ₂ , thick film	AuPd	300	Ethanol, 10 ppm	40	[128]
SnO ₂ , thick film	–	300	CH ₄ , 1000 ppm	12	[128]
SnO ₂ , thick film	Au	300	CH ₄ , 1000 ppm	30	[128]
SnO ₂ , thick film	Pd	300	CH ₄ , 1000 ppm	90	[128]
SnO ₂ , thick film	AuPd	300	CH ₄ , 1000 ppm	12	[128]
SnO ₂ , thick film	–	350	CO, 20 ppm	3	[136]
SnO ₂ , thick film	Au	225	CO, 20 ppm	5	[136]
SnO ₂ , thick film	Pd	100	CO, 20 ppm	3	[136]
SnO ₂ , thick film	AuPd	350	CO, 20 ppm	9	[136]

Table 2. Cont.

Supporting MOX, Morphology	Functionalization	T (°C)	Gas, Concentration	S	Ref.
SnO ₂ , thick film	–	500	CH ₄ , 50 ppm	3	[136]
SnO ₂ , thick film	Au	450	CH ₄ , 50 ppm	4.5	[136]
SnO ₂ , thick film	Pd	450	CH ₄ , 50 ppm	3	[136]
SnO ₂ , thick film	AuPd	400	CH ₄ , 50 ppm	6.5	[136]
SnO ₂ , thick film	–	375	NH ₃ , 10 ppm	2	[136]
SnO ₂ , thick film	Au	350	NH ₃ , 10 ppm	4	[136]
SnO ₂ , thick film	Pd	350	NH ₃ , 10 ppm	2	[136]
SnO ₂ , thick film	AuPd	350	NH ₃ , 10 ppm	6	[136]
SnO ₂ , nanosheet network	–	300	Acetone, 50 ppm	20	[137]
SnO ₂ , nanosheet network	Au	275	Acetone, 50 ppm	80	[137]
SnO ₂ , nanosheet network	Pd	250	Acetone, 50 ppm	40	[137]
SnO ₂ , nanosheet network	AuPd	250	Acetone, 50 ppm	110	[137]
WO ₃ , nanowire network	–	300	n-butanol, 100 ppm	26	[138]
WO ₃ , nanowire network	Pd	200	n-butanol, 100 ppm	69	[138]
WO ₃ , nanowire network	AuPd	200	n-butanol, 100 ppm	93	[138]

4.4.2. Functionalization with Metal Oxide Nanoparticles

Concerning the use of MOX nanostructures as catalysts, their beneficial effects arise both from the catalytic properties of the additive and from the formation of electrical junctions between the two MOX semiconductors.

CuO is a p-type semiconductor and the formation of p-n junctions at the interface with n-type MOX is often indicated as one of the key reasons for the observed enhanced sensitivity with respect to the pure n-type MOX. For example, this is the case of ethanol sensing with pristine and CuO-functionalized SnO₂ hollow spheres [61]. In addition, CuO catalyst is particularly effective for H₂S detection, which is probably its most popular use in gas sensing [140]. This is thanks to the suitability of CuO to react with H₂S forming CuS according to the reaction $\text{CuO} + \text{H}_2\text{S} \rightarrow \text{CuS} + \text{H}_2\text{O}$, which is reversible in an oxygen-rich environment [141]. Considering the metallic character of CuS, the p-n junction formed at the CuO–MOX interface is turned into a metal–semiconductor junction upon H₂S exposure, resulting in a very effective transduction mechanism. This mechanism is reported as being specific to H₂S. Indeed, as shown in Table 3, large H₂S response enhancements have been published for SnO₂–CuO composites based both on nanoparticles and nanowires as supporting material, while weaker enhancements have been indicated for other compounds such as CO and NH₃ [46,141].

In addition to p-n junctions, n-n junctions have been exploited. A remarkable example is given by SnO₂ and ZnO, which are widely used as individual material in a variety of morphologies, but they are also used combined with one another. Hierarchical morphologies are also widely employed to combine the beneficial morphological and functionalization effects. Concerning nanoparticle-shaped crystallites, SnO₂ nanofibers increased their response to ethanol and acetone by a factor of about three when decorated with ZnO nanoparticles [64]. This is thanks to the combined morphological effect, arising from the hierarchical structure, and the functionalization one. Porous opals with 1:1 SnO₂–ZnO composition were also realized [142]. In this case, the response to acetone was increased with respect to the same morphology realized with a single component, SnO₂ or ZnO, while for ethanol the composite material featured a response comparable with the one exhibited by pure SnO₂ and larger than the pure ZnO response, hence also providing benefits in terms of partial selectivity.

Concerning nanowires, Zhao et al. studied the effect of SnO₂-nanoparticle loading over the surface of ZnO nanowires for NO₂ detection. Their results indicated that the functionalization improves the response intensity to NO₂ by a factor of about six with respect to the performance of pristine ZnO [143]. NO₂ was also the target gas for SnO₂ nanowires cofunctionalized with ZnO nanoparticles and Pd nanoparticles, finding a nearly 3-times increase in the response of the composite material with respect to the base SnO₂ nanowires [144].

Table 3. Chemiresistors based on metal oxide (MOX) nanostructures functionalized with metal oxide nanoparticles. The response intensity S is calculated as $S = R_{\text{air}}/R_{\text{gas}}$ for reducing gases and as $S = R_{\text{gas}}/R_{\text{air}}$ for NO₂ at the sensor temperature (T). Gas concentrations are expressed in parts per million (ppm). In those cases in which information is not available from the original reference, the related cell reports ‘na’.

Supporting MOX, Morphology	Functionalization	T (°C)	Gas, Concentration	S	Ref.
SnO ₂ , hollow spheres	–	300	Ethanol, 300 ppm	11	[61]
SnO ₂ , hollow spheres	CuO	300	Ethanol, 300 ppm	35	[61]
SnO ₂ , thick film	–	350	H ₂ S, 2 ppm	100	[46]
SnO ₂ , thick film	CuO	200	H ₂ S, 2 ppm	600	[46]
SnO ₂ , thick film	–	350	CO, 40 ppm	3	[46]
SnO ₂ , thick film	CuO	350	CO, 40 ppm	4	[46]
SnO ₂ , thick film	–	300	NH ₃ , 20 ppm	2	[46]
SnO ₂ , thick film	CuO	250	NH ₃ , 20 ppm	2	[46]
SnO ₂ , nanowire network	–	400	H ₂ S, 2 ppm	8	[141]
SnO ₂ , nanowire network	CuO	200	H ₂ S, 2 ppm	3261	[141]
SnO ₂ , nanowire network	–	na	CO, 50 ppm	7	[141]
SnO ₂ , nanowire network	CuO	na	CO, 50 ppm	7	[141]
SnO ₂ , nanowire network	–	na	NH ₃ , 17 ppm	4	[141]
SnO ₂ , nanowire network	CuO	na	NH ₃ , 17 ppm	4	[141]
SnO ₂ , single nanowire	–	250	H ₂ S, 10 ppm	1.5	[141]
SnO ₂ , single nanowire	CuO	250	H ₂ S, 10 ppm	26	[141]
SnO ₂ , porous fiber	–	260	Ethanol, 100 ppm	120	[64]
SnO ₂ , porous fiber	ZnO	260	Ethanol, 100 ppm	360	[64]
SnO ₂ , porous fiber	–	260	Acetone, 100 ppm	10	[64]
SnO ₂ , porous fiber	ZnO	260	Acetone, 100 ppm	30	[64]
SnO ₂ , porous opal	–	250	Acetone, 100 ppm	13	[142]
SnO ₂ /ZnO, porous opal	–	275	Acetone, 100 ppm	45	[142]
ZnO, porous opal	–	350	Acetone, 100 ppm	17	[142]
SnO ₂ , porous opal	–	250	Ethanol, 100 ppm	22	[142]
SnO ₂ /ZnO, porous opal	–	250	Ethanol, 100 ppm	23	[142]
ZnO, porous opal	–	325	Ethanol, 100 ppm	12	[142]
SnO ₂ , nanowire network	–	300	NO ₂ , 5 ppm	2	[144]
SnO ₂ , nanowire network	Pd	300	NO ₂ , 5 ppm	4	[144]
SnO ₂ , nanowire network	ZnO	300	NO ₂ , 5 ppm	4	[144]
SnO ₂ , nanowire network	ZnO + Pd	300	NO ₂ , 5 ppm	6	[144]

4.4.3. Core–Shell Nanostructures

The exploitation of the MOX/MOX interface is also at the basis of core–shell nanostructures, in which the inner nanowire material (core) is completely coated by the shell layer, which typically has a polycrystalline structure. An example is reported in Figure 7, with reference to a SnO₂-ZnO core–shell sample. In this type of nanostructure, the outer layer is usually compact, and the composite material exposes the shell material to the gaseous environment. From the functional point of view, this is particularly evident in the case of core–shell nanostructures composed by a p-n (or n-p) couple of semiconductors, for which the sensing mechanism of the core is clearly distinguishable from that of the shell [145,146]. The transduction mechanism of the composite is strongly dependent on the core–shell electrical coupling, which in turn depends on the shell thickness. Investigations carried out with different nanowire-core/polycrystalline-shell systems, including CuO/ZnO [145], SnO₂/Cu₂O [146] and SnO₂/ZnO [147], indicated that the sensing response is optimized for a shell thickness approaching the Debye length (λ_D). The explanation of these results is typically carried out starting from the band structure of the two materials in contact with one another, assuming both materials are thick enough to restore the bulk properties outside the space-charge layer [145,147–149]. Figure 7 reports an example of this band structure using SnO₂-ZnO as a reference system. Starting from this framework, thickness arguments can be further briefly discussed as follows [147]: decreasing the shell thickness increases the sensitivity of the shell material to the interaction with gases, according to space-charge-layer arguments similar to those described in Section 3.2. Nonetheless, as the shell is thinned, an increasing amount of electrical transport takes place in the core instead of in the shell, thus decreasing its coupling with gas interaction occurring at the external surface of the shell. These results have been reported to apply in general to reducing gases and to core–shell systems, whichever their n-n, p-n or n-p character [145–147]. Such a general improvement, with poor specificity among reducing compounds, has also been confirmed by other authors [149]. The Ga₂O₃/SnO₂ system has also been exploited in the core–shell configuration, obtaining a reduction in the optimal temperature for ethanol detection with respect to the pristine Ga₂O₃ nanowire (400 vs. 600 °C) [150].

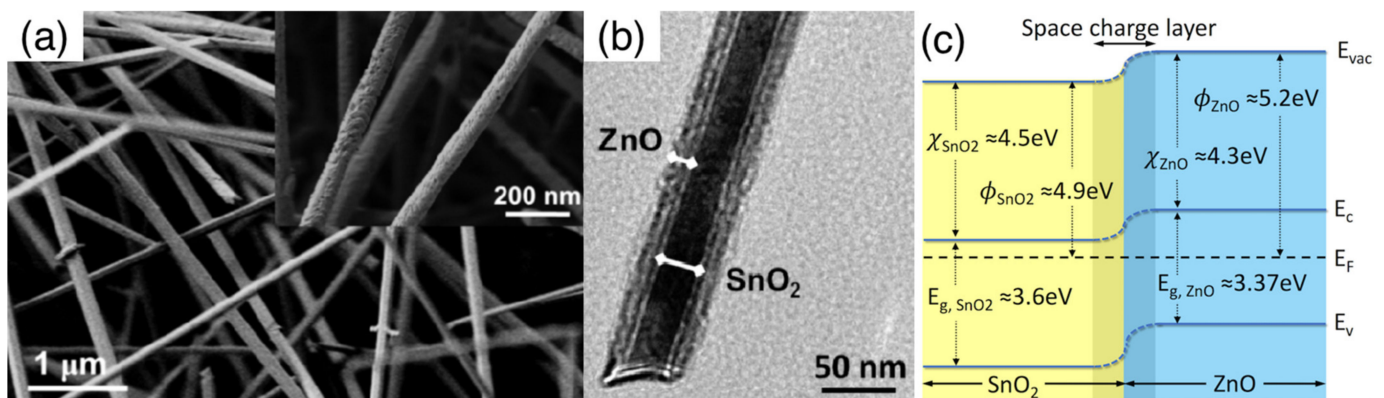


Figure 7. SEM (a) and TEM (b) images of SnO₂-ZnO core–shell composite material and the schematic representation of the band structure for the SnO₂-ZnO system (c). For both materials, the bulk values of their energy gap (E_g), work function (ϕ), electron affinity (χ) are reported; profiles of the vacuum (E_{vac}), valence band (E_v), conduction band (E_c) and Fermi level (E_F) energies are also schematically reported. Figure 7a,b are reprinted from [148].

Joint functionalization with MOX and with metallic nanoparticles is also reported in the literature. For example, a partial specificity to triethylamine was obtained by further functionalizing the ZnO-SnO₂ core–shell composite with Au nanoparticles, which allows to jointly exploit the gas specificity of the catalyst and beneficial effects of the core–shell structure on the transduction mechanism [149].

The sensing properties of these materials are resumed in Table 4 in terms of sensor response intensity S and type of sensing mechanism (n- vs. p-type).

Table 4. Chemiresistors based on metal oxide (MOX) core-shell nanostructures. The response intensity S is calculated as $S = R_{\text{gas}}/R_{\text{air}}$ for NO_2 and as $S = R_{\text{air}}/R_{\text{gas}}$ for other compounds in the case of n-type sensing response. The contrary is in the case of p-type sensing response. The n- or p- type response is reported in the S column. Gas concentrations are expressed in parts per million (ppm) and the sensor temperature is T .

Core MOX, Morphology	Shell MOX	T (°C)	Gas, Concentration	S (type)	Ref.
CuO, nanowire network	–	300	CO, 1 ppm	2.2 (p)	[145]
CuO, nanowire network	ZnO	300	CO, 1 ppm	6 (p)	[145]
ZnO, nanowire network	–	300	CO, 1 ppm	1.3 (n)	[145]
CuO, nanowire network	–	300	C_6H_6 , 1 ppm	2.3 (p)	[145]
CuO, nanowire network	ZnO	300	C_6H_6 , 1 ppm	5.8 (p)	[145]
ZnO, nanowire network	–	300	C_6H_6 , 1 ppm	2.3 (n)	[145]
SnO_2 , nanowire network	–	300	C_7H_8 , 10 ppm	2 (n)	[146]
SnO_2 , nanowire network	Cu_2O	300	C_7H_8 , 10 ppm	12 (p)	[146]
SnO_2 , nanowire network	–	300	C_6H_6 , 10 ppm	2 (n)	[146]
SnO_2 , nanowire network	Cu_2O	300	C_6H_6 , 10 ppm	13 (p)	[146]
SnO_2 , nanowire network	–	300	NO_2 , 10 ppm	130 (n)	[146]
SnO_2 , nanowire network	Cu_2O	300	NO_2 , 10 ppm	2 (p)	[146]
SnO_2 , nanowire network	–	300	CO, 10 ppm	5 (n)	[147]
SnO_2 , nanowire network	ZnO	300	CO, 10 ppm	80 (n)	[147]
SnO_2 , nanowire network	–	300	C_6H_6 , 10 ppm	5 (n)	[147]
SnO_2 , nanowire network	ZnO	300	C_6H_6 , 10 ppm	80 (n)	[147]
SnO_2 , nanowire network	–	300	NO_2 , 10 ppm	160 (n)	[147]
SnO_2 , nanowire network	ZnO	300	NO_2 , 10 ppm	25 (n)	[147]
ZnO, nanowire network	–	40	Triethylamine, 50 ppm	4 (n)	[149]
ZnO, nanowire network	SnO_2	40	Triethylamine, 50 ppm	7 (n)	[149]
ZnO, nanowire network	$\text{SnO}_2 + \text{Au}$	40	Triethylamine, 50 ppm	12 (n)	[149]
ZnO, nanowire network	–	40	Acetone, 500 ppm	2 (n)	[149]
ZnO, nanowire network	SnO_2	40	Acetone, 500 ppm	5 (n)	[149]
ZnO, nanowire network	$\text{SnO}_2 + \text{Au}$	40	Acetone, 500 ppm	6 (n)	[149]
ZnO, nanowire network	–	40	Ethanol, 50 ppm	2 (n)	[149]
ZnO, nanowire network	SnO_2	40	Ethanol, 50 ppm	4 (n)	[149]
ZnO, nanowire network	$\text{SnO}_2 + \text{Au}$	40	Ethanol, 50 ppm	6 (n)	[149]
Ga_2O_3 , nanowire network	–	600	Ethanol, 1000 ppm	100 (n)	[150]
Ga_2O_3 , nanowire network	SnO_2	400	Ethanol, 1000 ppm	65 (n)	[150]

4.4.4. Hierarchical, Branched Nanostructures

An additional opportunity offered by nanowires, which does not find an equivalent in the nanoparticle case, is the possibility to grow branched heterostructures composed by a nanowire backbone, with other nanowires extending from its surface. This is a very interesting configuration because it allows at the same time for the exploitation of more phenomena described in the previous sections. An example of this morphology is shown in Figure 8a. The two main features of this particular type of hierarchical structure

for gas sensing are: (i) the very open structure, which enhances the utility factor, and (ii) the MOX–MOX interface, which may be in the core–shell form or as dispersed branches growing out from the backbone nanowire, providing the functionalities already introduced in Sections 4.4.2 and 4.4.3, respectively.

Using the SnO₂–ZnO system as a case study, Tharsika et al. compared the performance of three different morphologies, namely the SnO₂ nanowire network in its pristine form, the same base material in a core–shell configuration using a ZnO film coating (Figure 7) and in a hierarchical configuration in which branched ZnO nanorods grow out the ZnO shell. Results indicate that this latter configuration is the most effective both in terms of response intensity to different compounds and in terms of partial selectivity to ethanol [148]. The Cu_xO–ZnO system has also been investigated as a branched structure for acetone sensing, obtaining a response about four times larger with respect to the individual nanowires [151]. In this case, ZnO branches are also not dispersed over the Cu_xO backbone but directly emerge from a uniform ZnO shell coating the underlying Cu_xO nanowire core. The response type indeed switches from p- to n-type as the backbone is coated by ZnO.

Branched nanowire heterostructures have also been exploited as hierarchical support for further functionalization with metallic or MOX nanoparticles. For example, the structure composed by SnO₂ nanowire as backbone, dispersed Bi₂O₃ branches and Pt nanoparticles has been used to detect NO₂ at sub-ppm levels [152]. The branched nanostructure (without Pt functionalization) revealed the best performance, with optimal performances reached at the working temperature of 300 °C owing to the SnO₂–Bi₂O₃ interface exposed to gases. Benefits arising from the addition of Pt consisted in reducing the optimal temperature to 50 °C for an almost room-temperature sensing [152]. Other branched, ternary materials have also been studied for NO₂ sensing. These are hierarchical structures composed by branched ZnO nanorods grown over SnO₂ nanowire and further functionalized with either Au [153] or Cr₂O₃ [154] nanoparticles. As for the SnO₂–ZnO–Au system, optimal performances were obtained at the working temperature of 300 °C, with the response of the ternary compound being about four times larger than the response of the branched nanostructure without Au nanoparticles and about six times the response of pristine SnO₂ nanowires. The increase is even larger for the SnO₂–ZnO–Cr₂O₃ system, its response to NO₂ being about ten and twenty times the response of the branched SnO₂–ZnO and the pure SnO₂ nanowires. These results were ascribed to the synergic effects of the branched structure of SnO₂–ZnO hierarchical support, their n–n interfaces and the effects of Au and Cr₂O₃, which act through the electronic and chemical sensitization mechanisms discussed in Section 4.4.1 [153,154].

Doping has also been used in conjunction with branched nanostructures. For example, branched SnO₂ nanowires were grown over metallic Sb-doped SnO₂, realizing a hierarchical structure characterized by semiconductor–metal interfaces. This system was used for ethanol sensing [155].

The response intensities *S* and the type of sensing mechanisms of the branched nanostructures discussed in this section are compared with those of the respective backbone nanostructures in Table 5.

Table 5. Chemiresistors based on branched metal oxide (MOX) nanostructures. The response intensity *S* is calculated as $S = R_{\text{gas}}/R_{\text{air}}$ for NO₂ and as $S = R_{\text{air}}/R_{\text{gas}}$ for other compounds in the case of n-type sensing response. The contrary is in the case of p-type sensing response. The n- or p-type response is reported in the *S* column. Gas concentrations are expressed in parts per million (ppm) and the sensor temperature is *T*.

Backbone MOX	Coating, Morphology	<i>T</i> (°C)	Gas, Concentration	<i>S</i> (type)	Ref.
SnO ₂	ZnO, shell	400	Ethanol, 20 ppm	20 (n)	[148]
SnO ₂	ZnO, shell + branch	400	Ethanol, 20 ppm	32 (n)	[148]
Cu _x O	–	250	Acetone, 50 ppm	1.2 (p)	[151]

Table 5. Cont.

Backbone MOX	Coating, Morphology	T (°C)	Gas, Concentration	S (type)	Ref.
Cu _x O	ZnO, shell	250	Acetone, 50 ppm	1.5 (n)	[151]
Cu _x O	ZnO, shell + branch	250	Acetone, 50 ppm	6.5 (n)	[151]
SnO ₂	–	50	NO ₂ , 1 ppm	–	[152]
SnO ₂	Bi ₂ O ₃ branch	50	NO ₂ , 1 ppm	3 (n)	[152]
SnO ₂	Bi ₂ O ₃ branch + Pt nanoparticles	50	NO ₂ , 1 ppm	28 (n)	[152]
SnO ₂	–	250	NO ₂ , 1 ppm	10 (n)	[152]
SnO ₂	Bi ₂ O ₃ branch	250	NO ₂ , 1 ppm	50 (n)	[152]
SnO ₂	Bi ₂ O ₃ branch + Pt nanoparticles	250	NO ₂ , 1 ppm	–	[152]
SnO ₂	–	300	NO ₂ , 20 ppm	2 (n)	[153]
SnO ₂	ZnO branch	300	NO ₂ , 20 ppm	4 (n)	[153]
SnO ₂	ZnO branch + Au nanoparticles	300	NO ₂ , 20 ppm	13 (n)	[153]
SnO ₂	–	300	NO ₂ , 10 ppm	2 (n)	[154]
SnO ₂	ZnO branch	300	NO ₂ , 10 ppm	5 (n)	[154]
SnO ₂	ZnO branch + Cr ₂ O ₃ nanoparticles	300	NO ₂ , 10 ppm	58 (n)	[154]
Sb-doped SnO ₂	SnO ₂ , branched	300	Ethanol, 100 ppm	51 (n)	[155]

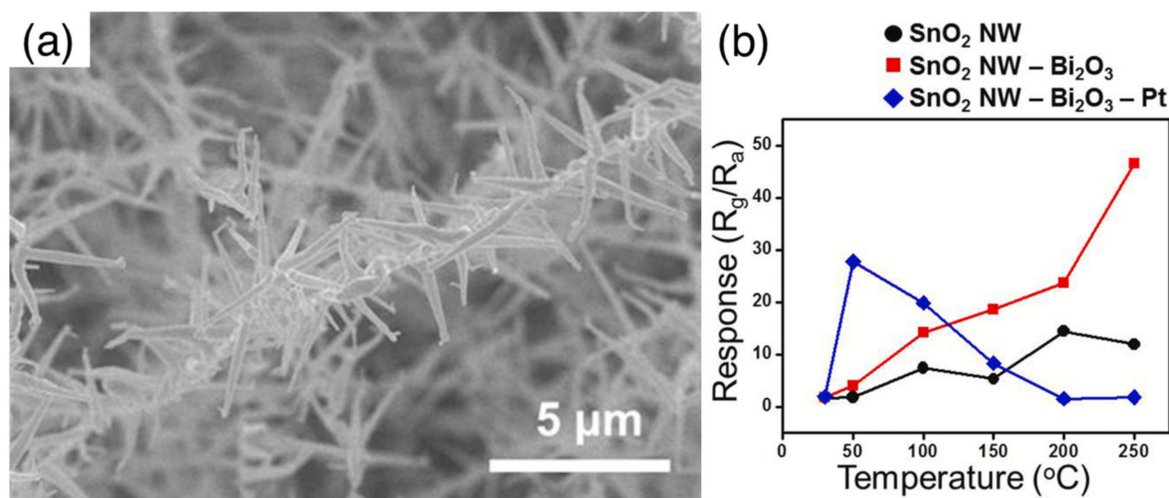


Figure 8. Branched hierarchical nanowires. SEM image of branched Bi₂O₃ nanowires grown over SnO₂ nanowires (a). Sensor response to 1 ppm of NO₂ vs. temperature for the branched Bi₂O₃–SnO₂ nanowires functionalized with Pt nanoparticles, branched Bi₂O₃–SnO₂ nanowires and the backbone SnO₂ nanowires (b). Figure 8a,b are reprinted from [152], Copyright (2021) with permission from Elsevier.

4.5. Inorganic–Organic Heterostructures

In addition to inorganic materials, organic layers have also been considered to functionalize metal oxides. The goal is to exploit the variety of interactions offered by the organic chemistry to control the sensitivity and the partial selectivity of the composite material.

4.5.1. Graphene and Related Materials

Nowadays, talking about organic functionalization immediately recalls graphene (G) and related materials such as graphene oxide (GO) and reduced graphene oxide (RGO). Indeed, several works have been published exploiting both nanoparticles, nanowires and

hierarchical nanostructures coupled with these carbon-based materials. Similarly to other functional interfaces mentioned in the previous sections, the electrical coupling between the two materials is a fundamental concept to explain the gas-sensing properties of the composite. For 2D materials, the band structure is depicted through Dirac cones, with the Fermi level and the shape of cones strongly depending on defects and number of layers, as well as bending and corrugation that may affect the 2D film [156]. These parameters, in turn, exhibit a large dependence from the synthesis conditions of the carbon-based material and from the morphological features of the surface over which it is deposited/synthesized. As a consequence, the electrical properties of these materials are still the subject of study and a unified picture is still to be achieved, especially for those situations in which many of the aforementioned effects may be involved at the same time, as is the case in gas-sensor devices.

In addition, G, GO and RGO are intrinsically sensitive to gases, hence they may also directly contribute to the overall response of the device [157,158].

The result is a large number of parameters that may be tuned to control the sensing properties of the composite material.

An example of hybrid material composed by ZnO nanorods and RGO sheets is reported in Figure 9a. At the interface between the two materials, electrical coupling gives rise to the formation of p-n inorganic–organic junctions, which are adopted to interpret the electrical and sensing properties of the composite. Figure 9b reports the schematic representation of the band structure of the RGO-ZnO interface in three conditions: the two separated materials, the coupled materials exposed to air and the coupled materials exposed to NO₂. Considering the work functions of RGO ($\approx 4.4\text{--}5$ eV) and of ZnO ($\approx 4.2\text{--}4.3$ eV), the alignment of the Fermi levels implies electrons transferring from ZnO to RGO, hence a depletion layer extending inside the ZnO nanorods [159]. Already at low RGO concentrations, this material was proposed to facilitate the electrical transport between connected nanorods owing to the reduced resistance of RGO with respect to the ZnO-ZnO interface. On the other hand, considering the low RGO concentration in the optimal device, the sensing mechanism was interpreted as the NO₂ molecules adsorbing mainly on ZnO. The proposed transduction mechanism involved the consequent downshift of the ZnO Fermi level, which in turn resulted in the electrons' withdrawal from the RGO phase and the hole concentration increase therein. This explained the experimentally observed p-type response (electrical resistance decrease upon gas exposure) of the system at room temperature [159]. On the other hand, n-type sensing is also reported in the literature for the RGO–ZnO system. For example, this is the case with ZnO hierarchical spheres composed of elementary nanoparticles deposited over RGO [160,161].

P-type response and room-temperature sensitivity were also reported for RGO functionalized with ZnO nanowires exposed to ammonia [162] and for RGO layers functionalized with hierarchical ZnO sheets composed by elementary nanoparticles exposed to NO₂ [163]. In this latter case, the p-type conductivity of the RGO phase was suggested as the motivation of the p-type sensing mechanism exhibited by the composite, whose intensity is further enhanced by interface effects. A similar mechanism may be inferred for the first case owing to the large amount (about 50% wt) of RGO.

The transition from n- to p-type sensing was observed in NH₃ sensing with an RGO-loaded SnO₂ film as the RGO load was increased [164].

SnO₂ nanowires have also been used with RGO for H₂S sensing at room temperature. In this case, the functionalization process left Cu contamination, and this was proposed as an important feature for the observed selective response to H₂S [165]. Tests carried out with other compounds, including NO₂ and ethanol, indicated an n-type response, differently from the previously discussed ZnO-RGO system; however, in the SnO₂-RGO case, the presence of Cu may also have a relevant role for these compounds, not only for H₂S. Cu was intentionally added as dopant in the ZnO film of the RGO-ZnO composite for H₂S sensing at room temperature [166].

Room-temperature NO_2 sensing was also achieved with RGO-functionalized In_2O_3 nanorods [167]. In this case, the response was n-type and ascribed to a dominant role of the MOX nanowire, which is n-type, with the MOX-RGO interface having the role of promoting sensing capability at room temperature [167].

Nanowires have been further exploited in the form of hierarchical structures in conjunction with RGO. An example is given by hierarchical 3D mesocrystals composed by Cu_2O nanowires deposited over RGO [168]. The sensing mechanism is based on p-p junctions, which featured p-type responses to NO_2 at room temperature [168].

Numerical values of the measured responses S and the type of sensing mechanisms are resumed in Table 6.

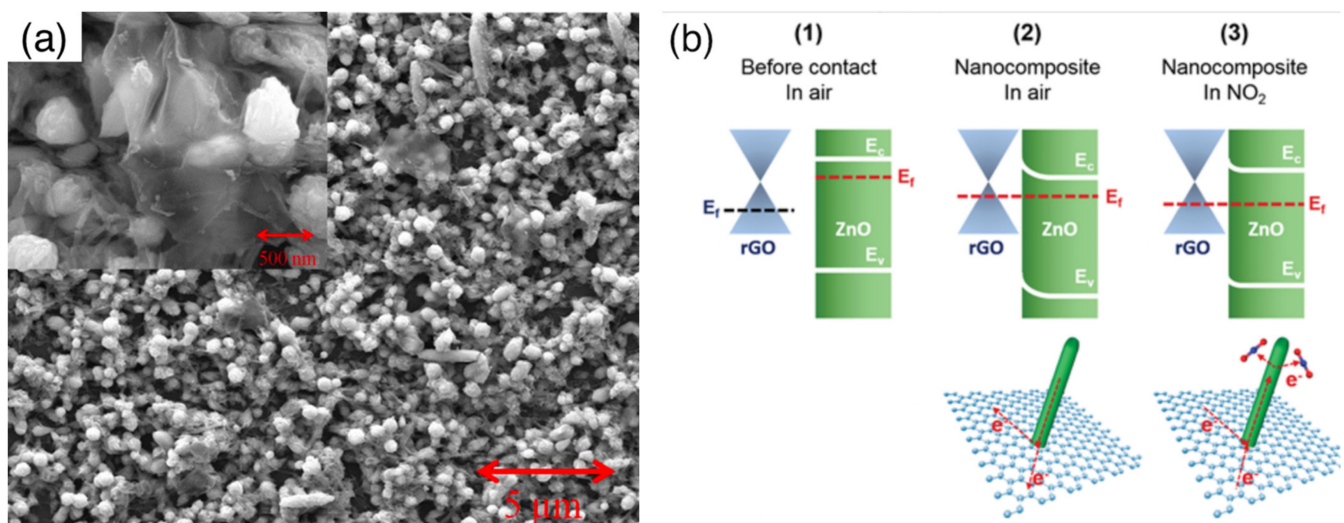


Figure 9. RGO–MOX interface. SEM image (top view) of the RGO–ZnO nanorods composite (a). Schematic representation of the electrical coupling mechanism between RGO and ZnO nanorods; energy bands are shown for the following three situations: disjointed materials, coupled materials exposed to air, and to NO_2 (b). Figure 9a is reprinted from [169], Copyright (2018) with permission from Elsevier. Figure 9b is reprinted with permission from [159], Copyright 2016 American Chemical Society.

An additional mode to exploit the RGO–MOX interface has been proposed by Van Quang et al. They deposited SnO_2 nanowires over both the electrodes of the device, leaving an empty gap between them (no nanowires between the electrodes). They further realized the connection between the two electrodes by means of a graphene sheet; in particular, the G sheet was not directly in contact with the metallic part of the electrodes but with the nanowires coating the electrodes. Owing to the metallic properties of graphene, the macroscopic electrical resistance of the device is given by the reversed biased junction formed at the G– SnO_2 nanowire interface [170]. Similarly to the solution proposed by Wei et al. [139] discussed in Section 4.4.1, the sensing response is governed by the modulation of the Schottky barrier formed at the metal–semiconductor interface. In particular, the proposed G– SnO_2 interface revealed the ability to detect NO_2 at the ppb level. At the optimal temperature (150°C), the device showed a response of about 6–50 ppb of NO_2 , which is comparable with the best performance reported in Table 1.

Before the advent of graphene and related materials, carbon was also widely exploited in the form of 1D carbon nanotubes. A recent article compared the SnO_2 -RGO and SnO_2 -CNT systems, in particular using semiconducting multiwalled CNTs. RGO functionalization revealed higher performance than that with CNTs, and this result was ascribed to the larger density of carbon–MOX interfaces for the 2D material. This enhancement was observed for SO_2 detection, while both types of functionalization revealed similar improvements with respect to the pristine SnO_2 using compounds such as CO and CH_4 [171]. The

motivation of this selectivity was not explained; it may reasonably arise from the complex dependence of both RGO and CNTs properties on their synthesis, defects, stresses and bending [172,173].

Table 6. Chemiresistors exploiting composite materials based on metal oxide (MOX) and 2D carbon nanostructures, namely graphene (G) and reduced graphene oxide (RGO). The response intensity S is calculated as $S = R_{\text{gas}}/R_{\text{air}}$ for NO_2 and as $S = R_{\text{air}}/R_{\text{gas}}$ for other compounds in the case of n-type sensing response. The contrary is in the case of p-type sensing response. The n- or p- type response is reported in the S column. In this column, ‘sb’ stands for the response arising from the metal–semiconductor Schottky barrier modulation (Equation (11)). Gas concentrations are expressed in parts per million (ppm); the sensor temperature is T ; ‘RT’ stands for ‘room temperature’.

MOX, Morphology	2D Carbon Material	T (°C)	Gas, Concentration	S (type)	Ref.
ZnO, nanorods	–	RT	NO_2 , 1 ppm	1.8 (n)	[159]
–	RGO	RT	NO_2 , 1 ppm	1.2 (p)	[159]
ZnO, nanorods	RGO	RT	NO_2 , 1 ppm	2.2 (p)	[159]
ZnO, nanosheets	–	RT	NO_2 , 50 ppm	6 (n)	[160]
ZnO, nanosheets	RGO	RT	NO_2 , 50 ppm	9 (n)	[160]
ZnO, hierarchical spheres	–	110	NO_2 , 1 ppm	4 (n)	[161]
ZnO, hierarchical spheres	RGO	110	NO_2 , 1 ppm	20 (n)	[161]
ZnO, hierarchical porous sheets	RGO	RT	NO_2 , 1 ppm	10 (p)	[163]
ZnO, nanoparticles	RGO	RT	NH_3 , 1 ppm	1.07 (p)	[162]
Cu doped SnO_2 , nanowires	RGO	RT	H_2S , 50 ppm	33 (n)	[165]
Cu doped SnO_2 , nanowires	RGO	RT	NH_3 , 50 ppm	1.25 (n)	[165]
Cu doped SnO_2 , nanowires	RGO	RT	NO_2 , 50 ppm	1.5 (n)	[165]
Cu doped ZnO, nanorods	RGO	RT	H_2S , 50 ppm	1.05 (p)	[166]
In_2O_3 , nanorods	RGO	RT	NO_2 , 97 ppm	2.5 (n)	[167]
Cu_2O , hierarchical mesocrystals	–	RT	NO_2 , 2 ppm	1.4 (p)	[168]
–	RGO	RT	NO_2 , 2 ppm	1.2 (p)	[168]
Cu_2O , hierarchical mesocrystals	RGO	RT	NO_2 , 2 ppm	1.7 (p)	[168]
SnO_2 , nanowire	G	RT	NO_2 , 0.1 ppm	11 (sb)	[170]

4.5.2. Organic Receptors

In addition to carbon allotropes and their (partially)oxidized nanostructures, other organic materials have been exploited to functionalize the MOX support.

For example, ZnO functionalization was studied with tris(hydroxymethyl)aminomethane (THMA). The supporting material was a network of ZnO nanowires, over which a coating of dispersed ZnO nanoparticles was applied. Nanoparticles were fundamental to increase the surface area of the supporting ZnO layer available for the THMA molecules with respect to the case of ZnO nanowires [174]. Indeed, the responses to NO_2 recorded with ZnO nanowires directly functionalized with THMA were quite similar to those recorded with the pristine oxide, while an increase of about two times was observed with the intermediate nanoparticle layer [174].

Recently, organosiloxanes have also been employed as organic coatings for acetone detection. A three- and a five-fold enhancement with respect to the pristine ZnO nanowire network were obtained using 3-glycidoxypropyltrimethoxysilane (GLYMO) and (3-aminopropyl)trimethoxysilane (APTMS), respectively [175]. As for GLYMO, the enhancement was ascribed to electronic and chemical sensitization. Similar to the mechanism described in Section 4.4, it arises from electrons transferring from the ZnO to the organic

layer owing to Fermi levels' alignment. Concerning APTMS, it also involves the receptor function of the device thanks to the ammine functional groups of APTMS. These groups remain available for interaction with gases and in particular with the carbon of acetone: $C_3H_6O + (NH_2)^- \Leftrightarrow (H_3C)_2-C=N + H_2O$, [175].

N-[3-(Trimethoxysilyl)propyl]ethylenediamine (en-APTAS 1) has been used to functionalize SnO₂ nanowires for NO₂ sensing, reaching a response of about 10 to 250 ppb [176]. From the calibration curve, a response of about 2 is extrapolated for the reference concentration of 50 ppb discussed in Section 4.1, which is comparable with the most performing NO₂ chemiresistors reported in the literature and resumed in Table 1.

Another important class of organic materials for gas sensing is the family of porphyrins. These materials have been widely exploited in the field, with optical and mass-sensitive transducing mechanisms often preferred to the electrical one owing to the poor conductivity of these materials [177]. To exploit the receptor functionalities of these organic materials through an electrical transduction mechanism, porphyrin-functionalized MOX chemiresistors working at room temperature have been developed, using visible light illumination to activate the electrical coupling between the supporting MOX and the receptor. These devices have been developed based on ZnO nanoparticles [178] and ZnO nanorods [179], showing the capability of the organic receptor to tune the sensitivity of the material to selected chemicals. For example, while pure ZnO revealed similar responses to ethanol and triethylamine, its functionalization with the H2TPPCOOH-porphyrin revealed suitability for increasing the partial selectivity in favor of the latter compound [179]. Such a capability was further exploited to discriminate off odors released by beef meat during the spoilage process [180].

The results discussed in this Section are resumed in Table 7.

Table 7. Chemiresistors based on metal oxide (MOX) nanostructures functionalized with organic molecules. The response intensity S is calculated as $S = R_{gas}/R_{air}$ for NO₂ and as $S = R_{air}/R_{gas}$ for other compounds in the case of n-type sensing response. The contrary is in the case of p-type sensing response. The n- or p- type response is reported in the S column. Gas concentrations are expressed in parts per million (ppm) or parts per billion (ppb) and the sensor temperature is T . (*): under solar illumination, (+): under UV illumination; (§): under visible light illumination.

MOX, Morphology	Organic Coating	T (°C)	Gas, Concentration	S (type)	Ref.
ZnO, nanowires	–	190	NO ₂ , 2 ppm	1.3 (n)	[174]
ZnO, nanowires	THMA	190	NO ₂ , 2 ppm	1.2 (n)	[174]
ZnO, nanowires + nanoparticles	–	190	NO ₂ , 2 ppm	1.22 (n)	[174]
ZnO, nanowires + nanoparticles	THMA	190	NO ₂ , 2 ppm	1.44 (n)	[174]
ZnO, nanowires	–	300	Acetone, 50 ppm	30 (n)	[175]
ZnO, nanowires	GLYMO	300	Acetone, 50 ppm	90 (n)	[175]
ZnO, nanowires	APTMS	300	Acetone, 50 ppm	160 (n)	[175]
SnO ₂ , nanowires	en-APTAS 1	RT (*)	NO ₂ , 250 ppb	10 (n)	[176]
ZnO, nanoparticles	H2TPPCOOH porphyrin	RT	Pentanol, 60 ppm	1.1 (n)	[178]
ZnO, nanorods	–	RT (+)	Ethanol, 10 ⁴ ppm	1.01 (p)	[179]
ZnO, nanorods	H2TPPCOOH porphyrin	RT (§)	Ethanol, 10 ⁴ ppm	1.002 (n)	[179]
ZnO, nanorods	–	RT (+)	Triethylamine, 10 ⁴ ppm	1.01 (p)	[179]
ZnO, nanorods	H2TPPCOOH porphyrin	RT (§)	Triethylamine, 10 ⁴ ppm	1.8 (n)	[179]

4.6. Self-Heating Effect

This working mode aims to exploit the current flowing through the sensitive layer to warm it by the Joule effect, without the use of an external heater. It was first tested in 2003 using a porous, polycrystalline film composed by μm-sized particles for CO detection [181].

At that time, besides the technological interest for the layout simplification achieved by avoiding the external heating element, the high density of grain boundaries intrinsic in the polycrystalline material was not effective in reducing power consumption. Indeed, the device required a power supply of the order of 1 W to activate CO sensing.

On the other hand, this idea revealed its full potential when it was tested with nanowire materials, in particular with chemiresistors based on a single-crystalline nanowire contacted by two electrodes. Indeed, as discussed in more detail in Sections 2 and 3, the nanowire is an excellent conductive channel for charge carriers thanks to its single crystalline structure, free from current-limiting elements such as grain boundaries [1]. Considering the small mass of the nanowire, a small current flowing through the nanowire itself is enough to heat it till the typical working temperature of gas sensors. To achieve a suitable self-heating effect, the device structure should also be designed to reduce heat dissipation as much as possible. Indeed, efficient self heating is typically achieved working with suspended nanowires, i.e., nanowires that are not in direct contact with the substrate but are separated from it by a gap of air [54]. A schematic representation of the suspended nanowire exploiting the self-heating mode is shown in Figure 10a. With this configuration, a few tens of μW (with currents of a few tens of μA) allow to reach the desired temperature [182]. Simulations for the temperature distribution along the suspended and the not-suspended nanowire is shown in Figure 10b [183]. The power consumption is lowered by about four orders of magnitude with respect to ordinary, bulky sensor substrates, whose power consumption is typically of the order of a few 100 mW, and by about 3 decades with respect to MEMS-based chemiresistors, which require a few 10 mW [184,185]. Such impressive power saving enables the development of sensing systems that are able to exploit the thermally activated reactions described in Section 3.1, and at the same time are energetically autonomous. For example, a proof-of-concept device was realized by coupling the self-heated chemiresistor with a thermoelectric microgenerator [186].

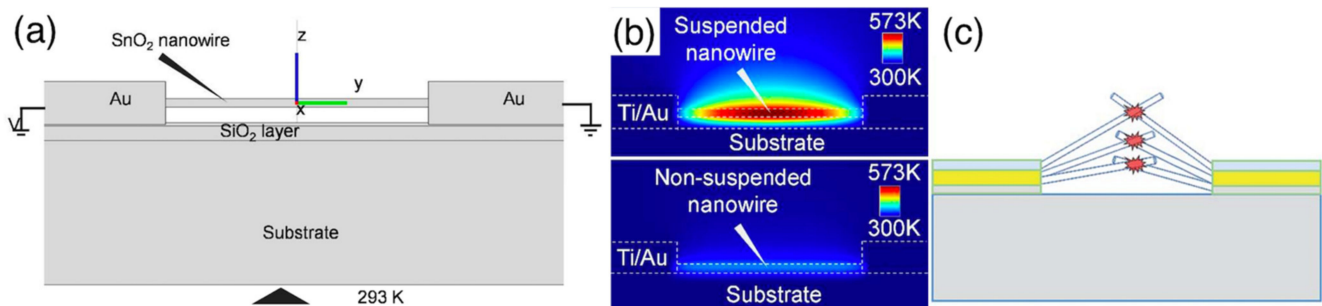


Figure 10. Self-heating. Schematic representation of the self-heating nanowire (a); simulation of temperature distribution along the nanowire for the suspended and not-suspended configurations (b); schematic representation of a self-heated nanowire network (c). Figure 10a,b are reprinted with permission from [183], Copyright 2016 American Chemical Society. Figure 10c is reproduced from Ref. [187] with permission from the Royal Society of Chemistry.

Despite the most effective exploitation of the self-heating effect being achieved with a single-nanowire device, interfaces have also been introduced in a controlled way to take advantage of their functional properties. For example, depositing nanowires with controlled density between two closely separated electrodes, the self-heating effect was exploited with a networked layer. Figure 10c shows the schematic representation of this type of self-heated device. The reduced gap between electrodes ($2\ \mu\text{m}$) and the wire morphology of the MOX nanostructures were important to ensure a network with a few crystallite–crystallite junctions, which are the current-limiting elements [187]. The reduced number of junctions allowed the exploitation of the self-heating effect to detect NO_2 with about $10\ \mu\text{W}$. Increasing the density of the network results in an increase in the required power supply to the order of 1 mW due to the larger number of junction elements [187].

Self heating was also exploited with composite metal oxides to merge the low power consumption with benefits arising from the heterointerfaces of the composite. As an example, a low-density network composed of ZnO nanowires coated with a SnO₂ shell and further functionalized by Pt nanoparticles was integrated in a device characterized by a short gap (a few μm) between the electrodes. The C₇H₈-sensing performance were optimized by tuning the ZnO coverage thickness, resulting in sub-ppm sensing capability with a power supply of about 30 μW [188].

Self-heated devices are also appealing owing to their fast thermal dynamics, which feature time constants of the order of ms [189], comparable with those exhibited by microhotplates [190]. This allows for the use of temperature-modulation techniques that have been widely investigated and exploited with both bulky and MEMS substrates to increase the selectivity of individual sensors [191,192]. Since the response of MOX strongly depends on the working temperature, the periodic modulation of this parameter allows the exploration of a range of different sensitivities and to emphasize the partial selectivity of MOX based on gas-interaction transients [193].

For example, a self-heated SnO₂ single nanowire was used to track the CO concentration in a background with different humidity levels using a square-wave bias characterized by a duty cycle of 50% and period of 1 s [194].

The fast thermal time constants exhibited by self-heated devices have also been exploited to further reduce power consumption from the μW range down to the pW level. In particular, applying a short bias pulse (a few ms) every few seconds to a single SnO₂ nanowire device, Meng et al. achieved sub-ppm sensing of NO₂ using less than 40 pW [183].

5. Conclusions

The main approaches to develop resistive gas sensors exploiting metal oxide nanowires have been reviewed. About 20 years have passed since the first publications proposing the use of these materials for chemosensing as an alternative to polycrystalline layers composed by nanoparticles. The goal of this paper is to review the results achieved so far in the field, starting from the structural and morphological features that attracted the attention of the scientific community since the early works.

The overall impression is for the most effective exploitation of the nanowire structure and morphology being achieved in terms of power-supply saving and utility-factor optimization.

Regarding the former, the best results have been obtained through the self-heating effect, which exploits the absence of grain boundaries in the single-nanowire device and the Joule effect to reach the temperature required to activate the gas-sensing mechanism. This is probably the most impressive result, since it offers the opportunity to reduce the power consumption by 3–4 orders of magnitude with respect to state-of-the-art MEMS-based chemiresistors, hence opening enormous potentialities for integration in portable devices, including smartphones, and the development of networks of energy-autonomous sensors. Its prospects are mainly in two directions: (i) device integration, i.e., the development of methodologies and processes to integrate these sensors into effective sensing systems, often exploiting the electronic nose and/or the temperature-modulation approach; (ii) lowering the preparation cost. The exploitation of nanowire networks with a low and well-controlled number of nanowire–nanowire junctions is particularly promising in this sense, allowing for a suitable compromise between power saving and ease of device fabrication, which is still unsatisfactory with the actual preparation technology of single-nanowire devices.

The latter is an intrinsic feature in nanowire mats, which are typically characterized by wide-open volumes between wires, suitable for an efficient gas diffusion. Nonetheless, it should be noted that porosity optimization is intrinsic but not unique for nanowire mats. Indeed, several papers reported successful results achieved with nanoparticle layers, both organized in hierarchical structures and traditional thick films. Unique to nanowires is the branched structure, a particular form of hierarchical architecture, which allows for the merging of the open structure of nanowire networks with the functional properties of the MOX–MOX interfaces. Apart from this particular configuration, functionalization has

not emerged as revealing something particular arising from the nanoparticle or nanowire morphology. Functionalization with metallic or metal oxide nanoparticles as well as organic materials has been applied with both types of MOX morphologies and may be used in combination with all the aforementioned configurations of nanowires to extend the possibilities to tune the sensing properties of the considered device. Especially concerning metallic and MOX catalysts, approaches traditionally developed with thick films as support are being further exploited and adapted for application with nanowire-based devices. Opportunities seem almost equally open for both nanowires and nanoparticles.

As for the different surface termination of nanowires and nanoparticles, flat vs. rounded, this was already highlighted in the first gas-sensing publications. Since then, it has been proposed as an appealing opportunity to merge the results of surface science, typically obtained by working with macroscopic single crystals, with those of applicative fields such as catalysis and gas sensing, which employ films composed by interconnected nanostructures. Despite the remarkable results obtained both in terms of sensor response and partial selectivity, a proper understanding of surface termination effects is still to be achieved and there is much room for both fundamental and device-oriented studies in order to reduce the gap between these two fields. The main results reviewed in the present paper are briefly summarized in Table 8.

Table 8. Resumed comparison between nanowires (NWs) and nanoparticles (NPs), relationship between the structural/morphological properties and the related gas-sensing phenomena and properties.

Single-Phase Materials		
Feature	Nanowires (NWs)	Nanoparticles (NPs)
Surface termination	Well-defined crystalline planes: <ul style="list-style-type: none"> • Receptor/transducer functions (response intensity and partial selectivity) related to specific crystalline planes. 	Rounded shape: <ul style="list-style-type: none"> • Receptor/transducer functions (response intensity and partial selectivity) related to spherical/irregular surfaces.
Length-to-diameter aspect ratio	Large, often >10: <ul style="list-style-type: none"> • Less effective than NPs in terms of surface-to-volume ratio and transducer function; • NW Network: open morphology for optimal diffusion (enhanced response intensity and diffusion-related partial selectivity owing to enhanced utility factor); • NW network: porosity does not decrease with decrease in the NW diameter; • Individual NW: no grain boundaries for improved stability (no grain coarsening); • Individual NW and low-density NW networks: self-heating effect for extremely low power consumption. 	Almost unitary, ≈ 1 : <ul style="list-style-type: none"> • Most effective morphology for optimization of surface-to-volume ratio and transducer function (transition from surface-to-volume depletion regimes as the NP diameter decreases); • Porosity may decrease with decrease in the NP diameter; • Large density of grain boundaries (elements featuring the most effective transducer function and preferential gas adsorption).
Doping	<ul style="list-style-type: none"> • Modulation of charge-carrier density (and Debye length); • Modulation of transducer and receptor functions. 	<ul style="list-style-type: none"> • Increased thermal stability owing to hindered grain-coarsening phenomena; • Possible dopant-induced phase transition.
Hierarchical structures	<ul style="list-style-type: none"> • More open morphology for optimal diffusion (enhanced response intensity and diffusion-related partial selectivity owing to enhanced utility factor); 	

Table 8. Cont.

Heterostructure-based materials		
Surface functionalization	Nanowires (NWs)	Nanoparticles (NPs)
metallic nanoparticles	<ul style="list-style-type: none"> Electronic and chemical sensitization for lowering optimal sensing temperature, increasing response intensity and partial selectivity. 	
MOX nanostructures	<ul style="list-style-type: none"> Exploitation of the interface and the additive sensing capabilities for enhanced response intensity and partial selectivity. Branched NW heterostructure merging the open hierarchical morphology with the interface and additive sensing capabilities. 	–
Organic materials	<ul style="list-style-type: none"> Exploitation of the interface and the additive sensing capabilities to reduce the optimal working temperature, enhancing the response intensity and the partial selectivity. 	

Funding: This research was funded by Fondazione Cariplo and Regione Lombardia through the project EMpowerment del PAzienTe In cAsa (EMPATIA@LECCO).

Institutional Review Board Statement: Not applicable.

Informed Consent Statement: Not applicable.

Data Availability Statement: Not applicable.

Conflicts of Interest: The authors declare no conflict of interest.

References

- Pan, Z.W.; Dai, Z.R.; Wang, Z.L. Nanobelts of Semiconducting Oxides. *Science* **2001**, *291*, 1947–1949. [[CrossRef](#)] [[PubMed](#)]
- Comini, E.; Faglia, G.; Sberveglieri, G.; Pan, Z.; Wang, Z.L. Stable and Highly Sensitive Gas Sensors Based on Semiconducting Oxide Nanobelts. *Appl. Phys. Lett.* **2002**, *81*, 1869–1871. [[CrossRef](#)]
- Banerjee, S.; Dan, A.; Chakravorty, D. Review Synthesis of Conducting Nanowires. *J. Mater. Sci.* **2002**, *37*, 4261–4271. [[CrossRef](#)]
- Cheng, C.; Fan, H.J. Branched Nanowires: Synthesis and Energy Applications. *Nano Today* **2012**, *7*, 327–343. [[CrossRef](#)]
- Manzano, C.V.; Philippe, L.; Serrà, A. Recent Progress in the Electrochemical Deposition of ZnO Nanowires: Synthesis Approaches and Applications. *Crit. Rev. Solid State Mater. Sci.* **2021**, *in press*. [[CrossRef](#)]
- Wang, M.C.P.; Gates, B.D. Directed Assembly of Nanowires. *Mater. Today* **2009**, *12*, 34–43. [[CrossRef](#)]
- Fan, Z.; Ho, J.C.; Takahashi, T.; Yerushalmi, R.; Takei, K.; Ford, A.C.; Chueh, Y.-L.; Javey, A. Toward the Development of Printable Nanowire Electronics and Sensors. *Adv. Mater.* **2009**, *21*, 3730–3743. [[CrossRef](#)]
- Adam, T.; Dhahi, T.S.; Gopinath, S.C.B.; Hashim, U. Novel Approaches in Fabrication and Integration of Nanowire for Micro/Nano Systems. *Crit. Rev. Anal. Chem.* **2021**, *in press*. [[CrossRef](#)]
- Milano, G.; Porro, S.; Valov, I.; Ricciardi, C. Recent Developments and Perspectives for Memristive Devices Based on Metal Oxide Nanowires. *Adv. Electron. Mater.* **2019**, *5*, 1800909. [[CrossRef](#)]
- Zhou, Z.; Lan, C.; Wei, R.; Ho, J.C. Transparent Metal-Oxide Nanowires and Their Applications in Harsh Electronics. *J. Mater. Chem. C* **2019**, *7*, 202–217. [[CrossRef](#)]
- Yang, B.; Myung, N.V.; Tran, T.-T. 1D Metal Oxide Semiconductor Materials for Chemiresistive Gas Sensors: A Review. *Adv. Electron. Mater.* **2021**, *7*, 2100271. [[CrossRef](#)]
- Cai, B.; Song, Z.; Tong, Y.; Tang, Q.; Shaymurat, T.; Liu, Y. A Single Nanobelt Transistor for Gas Identification: Using a Gas-Dielectric Strategy. *Sensors* **2016**, *16*, 917. [[CrossRef](#)]
- Xue, N.; Zhang, Q.; Zhang, S.; Zong, P.; Yang, F. Highly Sensitive and Selective Hydrogen Gas Sensor Using the Mesoporous SnO₂ Modified Layers. *Sensors* **2017**, *17*, 2351. [[CrossRef](#)]
- Xiao, B.; Wang, F.; Zhai, C.; Wang, P.; Xiao, C.; Zhang, M. Facile Synthesis of In₂O₃ Nanoparticles for Sensing Properties at Low Detection Temperature. *Sens. Actuators B Chem.* **2016**, *235*, 251–257. [[CrossRef](#)]
- Zhu, Z.; Suzuki, M.; Nagashima, K.; Yoshida, H.; Kanai, M.; Meng, G.; Anzai, H.; Zhuge, F.; He, Y.; Boudot, M.; et al. Rational Concept for Reducing Growth Temperature in Vapor-Liquid-Solid Process of Metal Oxide Nanowires. *Nano Lett.* **2016**, *16*, 7495–7502. [[CrossRef](#)]
- Klamchuen, A.; Suzuki, M.; Nagashima, K.; Yoshida, H.; Kanai, M.; Zhuge, F.; He, Y.; Meng, G.; Kai, S.; Takeda, S.; et al. Rational Concept for Designing Vapor-Liquid-Solid Growth of Single Crystalline Metal Oxide Nanowires. *Nano Lett.* **2015**, *15*, 6406–6412. [[CrossRef](#)]

17. Abokifa, A.A.; Haddad, K.; Fortner, J.; Lo, C.S.; Biswas, P. Sensing Mechanism of Ethanol and Acetone at Room Temperature by SnO₂ Nano-Columns Synthesized by Aerosol Routes: Theoretical Calculations Compared to Experimental Results. *J. Mater. Chem. A* **2018**, *6*, 2053–2066. [[CrossRef](#)]
18. Nguyen, K.; Hung, C.M.; Ngoc, T.M.; Thanh Le, D.T.; Nguyen, D.H.; Nguyen Van, D.; Nguyen Van, H. Low-Temperature Prototype Hydrogen Sensors Using Pd-Decorated SnO₂ Nanowires for Exhaled Breath Applications. *Sens. Actuators B Chem.* **2017**, *253*, 156–163. [[CrossRef](#)]
19. Hernandez-Ramirez, F.; Tarancon, A.; Casals, O.; Pellicer, E.; Rodriguez, J.; Romano-Rodriguez, A.; Morante, J.R.; Barth, S.; Mathur, S. Electrical Properties of Individual Tin Oxide Nanowires Contacted to Platinum Electrodes. *Phys. Rev. B* **2007**, *76*, 085429. [[CrossRef](#)]
20. Vomiero, A.; Ponzoni, A.; Comini, E.; Ferroni, M.; Faglia, G.; Sberveglieri, G. Direct Integration of Metal Oxide Nanowires into an Effective Gas Sensing Device. *Nanotechnology* **2010**, *21*, 145502. [[CrossRef](#)]
21. Klamchuen, A.; Yanagida, T.; Kanai, M.; Nagashima, K.; Oka, K.; Rahong, S.; Gang, M.; Horprathum, M.; Suzuki, M.; Hidaka, Y.; et al. Study on Transport Pathway in Oxide Nanowire Growth by Using Spacing-Controlled Regular Array. *Appl. Phys. Lett.* **2011**, *99*, 193105. [[CrossRef](#)]
22. Ho, S.-T.; Wang, C.-Y.; Liu, H.-L.; Lin, H.-N. Catalyst-Free Selective-Area Growth of Vertically Aligned Zinc Oxide Nanowires. *Chem. Phys. Lett.* **2008**, *463*, 141–144. [[CrossRef](#)]
23. Qin, Y.; Xie, W.; Liu, Y.; Ye, Z. Thermal-Oxidative Growth of Aligned W18O₄₉ Nanowire Arrays for High Performance Gas Sensor. *Sens. Actuators B Chem.* **2016**, *223*, 487–495. [[CrossRef](#)]
24. Steinhauer, S.; Brunet, E.; Maier, T.; Mutinati, G.C.; Köck, A.; Freudenberg, O.; Gspan, C.; Grogger, W.; Neuhold, A.; Resel, R. Gas Sensing Properties of Novel CuO Nanowire Devices. *Sens. Actuators B Chem.* **2013**, *187*, 50–57. [[CrossRef](#)]
25. Ponzoni, A.; Russo, V.; Bailini, A.; Casari, C.S.; Ferroni, M.; Li Bassi, A.; Migliori, A.; Morandi, V.; Ortolani, L.; Sberveglieri, G.; et al. Structural and Gas-Sensing Characterization of Tungsten Oxide Nanorods and Nanoparticles. *Sens. Actuators B Chem.* **2011**, *153*, 340–346. [[CrossRef](#)]
26. Zeng, H.; Zhang, G.; Nagashima, K.; Takahashi, T.; Hosomi, T.; Yanagida, T. Metal–Oxide Nanowire Molecular Sensors and Their Promises. *Chemosensors* **2021**, *9*, 41. [[CrossRef](#)]
27. Zhang, B.; Fu, W.; Meng, X.; Ruan, A.; Su, P.; Yang, H. Enhanced Ethanol Sensing Properties Based on Spherical-Coral-like SnO₂ Nanorods Decorated with α -Fe₂O₃ Nanocrystallites. *Sens. Actuators B Chem.* **2018**, *261*, 505–514. [[CrossRef](#)]
28. Kuchibhatla, S.V.N.T.; Karakoti, A.S.; Bera, D.; Seal, S. One Dimensional Nanostructured Materials. *Prog. Mater. Sci.* **2007**, *52*, 699–913. [[CrossRef](#)]
29. Jeon, J.-Y.; Park, S.-J.; Ha, T.-J. Functionalization of Zinc Oxide Nanoflowers with Palladium Nanoparticles via Microwave Absorption for Room Temperature-Operating Hydrogen Gas Sensors in the Ppb Level. *ACS Appl. Mater. Interfaces* **2021**, *13*, 25082–25091. [[CrossRef](#)]
30. Lv, Y.; Huang, K.; Zhang, W.; Ran, S.; Chi, F.; Yang, B.; Liu, X. High-Performance Gas-Sensing Properties of Octahedral NiO Crystals Prepared via One-Step Controllable Synthesis Route. *Cryst. Res. Technol.* **2014**, *49*, 109–115. [[CrossRef](#)]
31. Kooti, M.; Keshtkar, S.; Askarieh, M.; Rashidi, A. Progress toward a Novel Methane Gas Sensor Based on SnO₂ Nanorods-Nanoporous Graphene Hybrid. *Sens. Actuators B Chem.* **2019**, *281*, 96–106. [[CrossRef](#)]
32. Chang, C.-M.; Hon, M.-H.; Leu, I.-C. Outstanding H₂ Sensing Performance of Pd Nanoparticle-Decorated ZnO Nanorod Arrays and the Temperature-Dependent Sensing Mechanisms. *ACS Appl. Mater. Interfaces* **2013**, *5*, 135–143. [[CrossRef](#)] [[PubMed](#)]
33. Kim, T.; Lee, S.; Cho, W.; Kwon, Y.M.; Baik, J.M.; Shin, H. Development of a Novel Gas-Sensing Platform Based on a Network of Metal Oxide Nanowire Junctions Formed on a Suspended Carbon Nanomesh Backbone. *Sensors* **2021**, *21*, 4525. [[CrossRef](#)] [[PubMed](#)]
34. Fort, A.; Mugnaini, M.; Rocchi, S.; Vignoli, V.; Comini, E.; Faglia, G.; Ponzoni, A. Metal-Oxide Nanowire Sensors for CO Detection: Characterization and Modeling. *Sens. Actuators B Chem.* **2010**, *148*, 283–291. [[CrossRef](#)]
35. Barsan, N.; Weimar, U. Conduction Model of Metal Oxide Gas Sensors. *J. Electroceramics* **2001**, *7*, 143–167. [[CrossRef](#)]
36. Ponce, M.A.; Bueno, P.R.; Varela, J.; Castro, M.S.; Aldao, C.M. Impedance Spectroscopy Analysis of SnO₂ Thick-Films Gas Sensors. *J. Mater. Sci. Mater. Electron.* **2008**, *19*, 1169–1175. [[CrossRef](#)]
37. Vodolazskaya, I.V.; Eserkepov, A.V.; Akhunzhanov, R.K.; Tarasevich, Y.Y. Effect of Tunneling on the Electrical Conductivity of Nanowire-Based Films: Computer Simulation within a Core–Shell Model. *J. Appl. Phys.* **2019**, *126*, 244903. [[CrossRef](#)]
38. Ponzoni, A. The Contributions of Junctions and Nanowires/Nanotubes in Conductive Networks. *Appl. Phys. Lett.* **2019**, *114*, 153105. [[CrossRef](#)]
39. Gomes da Rocha, C.; Manning, H.G.; O’Callaghan, C.; Ritter, C.; Bellew, A.T.; Boland, J.J.; Ferreira, M.S. Ultimate Conductivity Performance in Metallic Nanowire Networks. *Nanoscale* **2015**, *7*, 13011–13016. [[CrossRef](#)]
40. Kim, D.; Nam, J. Analyzing Conducting Rod Networks Using Centrality. *Electrochim. Acta* **2021**, *370*, 137725. [[CrossRef](#)]
41. Lee, S.P. Electrodes for Semiconductor Gas Sensors. *Sensors* **2017**, *17*, 683. [[CrossRef](#)]
42. Zhang, Z.; Yao, K.; Liu, Y.; Jin, C.; Liang, X.; Chen, Q.; Peng, L.-M. Quantitative Analysis of Current–Voltage Characteristics of Semiconducting Nanowires: Decoupling of Contact Effects. *Adv. Funct. Mater.* **2007**, *17*, 2478–2489. [[CrossRef](#)]
43. Hernández-Ramírez, F.; Tarancón, A.; Casals, O.; Rodríguez, J.; Romano-Rodríguez, A.; Morante, J.R.; Barth, S.; Mathur, S.; Choi, T.Y.; Poulidakos, D.; et al. Fabrication and Electrical Characterization of Circuits Based on Individual Tin Oxide Nanowires. *Nanotechnology* **2006**, *17*, 5577–5583. [[CrossRef](#)]

44. Yamazoe, N. New Approaches for Improving Semiconductor Gas Sensors. *Sens. Actuators B Chem.* **1991**, *5*, 7–19. [[CrossRef](#)]
45. Yamazoe, N.; Shimano, K. Theory of Power Laws for Semiconductor Gas Sensors. *Sens. Actuators B Chem.* **2008**, *128*, 566–573. [[CrossRef](#)]
46. Krivetskiy, V.; Ponzoni, A.; Comini, E.; Badalyan, S.; Romyantseva, M.; Gaskov, A. Selectivity Modification of SnO₂-Based Materials for Gas Sensor Arrays. *Electroanalysis* **2010**, *22*, 2809–2816. [[CrossRef](#)]
47. Gurlo, A.; Bârsan, N.; Ivanovskaya, M.; Weimar, U.; Göpel, W. In₂O₃ and MoO₃-In₂O₃ Thin Film Semiconductor Sensors: Interaction with NO₂ and O₃. *Sens. Actuators B Chem.* **1998**, *47*, 92–99. [[CrossRef](#)]
48. Lantto, V.; Romppainen, P.; Leppävuori, S. A Study of the Temperature Dependence of the Barrier Energy in Porous Tin Dioxide. *Sens. Actuators* **1988**, *14*, 149–163. [[CrossRef](#)]
49. Sinkkonen, J. DC Conductivity of a Random Barrier Network. *Phys. Status Solidi* **1980**, *102*, 621–627. [[CrossRef](#)]
50. Ponzoni, A.; Comini, E.; Concina, I.; Ferroni, M.; Falasconi, M.; Gobbi, E.; Sberveglieri, V.; Sberveglieri, G. Nanostructured Metal Oxide Gas Sensors, a Survey of Applications Carried out at SENSOR Lab, Brescia (Italy) in the Security and Food Quality Fields. *Sensors* **2012**, *12*, 17023–17045. [[CrossRef](#)]
51. D'Amico, A.; Di Natale, C. A Contribution on Some Basic Definitions of Sensors Properties. *IEEE Sens. J.* **2001**, *1*, 183–190. [[CrossRef](#)]
52. Prades, J.D.; Jimenez-Diaz, R.; Manzanares, M.; Hernandez-Ramirez, F.; Cirera, A.; Romano-Rodriguez, A.; Mathur, S.; Morante, J.R. A Model for the Response towards Oxidizing Gases of Photoactivated Sensors Based on Individual SnO₂ nanowires. *Phys. Chem. Chem. Phys.* **2009**, *11*, 10881–10889. [[CrossRef](#)] [[PubMed](#)]
53. Sakai, G.; Matsunaga, N.; Shimano, K.; Yamazoe, N. Theory of Gas-Diffusion Controlled Sensitivity for Thin Film Semiconductor Gas Sensor. *Sens. Actuators B Chem.* **2001**, *80*, 125–131. [[CrossRef](#)]
54. Panchapakesan, B.; DeVoe, D.L.; Widmaier, M.R.; Cavicchi, R.; Semancik, S. Nanoparticle Engineering and Control of Tin Oxide Microstructures for Chemical Microsensor Applications. *Nanotechnology* **2001**, *12*, 336–349. [[CrossRef](#)]
55. Yamazoe, N.; Shimano, K. Roles of Shape and Size of Component Crystals in Semiconductor Gas Sensors: I. Response to oxygen. *J. Electrochem. Soc.* **2008**, *155*, J85. [[CrossRef](#)]
56. Yamazoe, N.; Shimano, K. Roles of Shape and Size of Component Crystals in Semiconductor Gas Sensors: II. Response to NO₂ and H₂. *J. Electrochem. Soc.* **2008**, *155*, J93. [[CrossRef](#)]
57. Hua, Z.; Qiu, Z.; Li, Y.; Zeng, Y.; Wu, Y.; Tian, X.; Wang, M.; Li, E. A Theoretical Investigation of the Power-Law Response of Metal Oxide Semiconductor Gas Sensors II: Size and Shape Effects. *Sens. Actuators B Chem.* **2018**, *255*, 3541–3549. [[CrossRef](#)]
58. Rebholz, J.; Bonanati, P.; Weimar, U.; Barsan, N. Grain Shape Influence on Semiconducting Metal Oxide Based Gas Sensor Performance: Modeling versus Experiment. *Anal. Bioanal. Chem.* **2014**, *406*, 3977–3983. [[CrossRef](#)]
59. Ottaviano, L.; Maccallini, E.; Santucci, S. Visualisation of the Preferential Adsorption Sites of Oxygen onto WO₃ Nano-Particles. *Surf. Sci.* **2001**, *492*, L700–L704. [[CrossRef](#)]
60. Lee, J.-H. Gas Sensors Using Hierarchical and Hollow Oxide Nanostructures: Overview. *Sens. Actuators B Chem.* **2009**, *140*, 319–336. [[CrossRef](#)]
61. Li, M.; Zhu, H.; Cheng, J.; Zhao, M.; Yan, W. Synthesis and Improved Ethanol Sensing Performance of CuO/SnO₂ Based Hollow Microspheres. *J. Porous Mater.* **2017**, *24*, 507–518. [[CrossRef](#)]
62. Liu, J.; Dai, M.; Wang, T.; Sun, P.; Liang, X.; Lu, G.; Shimano, K.; Yamazoe, N. Enhanced Gas Sensing Properties of SnO₂ Hollow Spheres Decorated with CeO₂ Nanoparticles Heterostructure Composite Materials. *ACS Appl. Mater. Interfaces* **2016**, *8*, 6669–6677. [[CrossRef](#)]
63. Motsoeneng, R.G.; Kortidis, I.; Rikhotso, R.; Swart, H.C.; Ray, S.S.; Motaung, D.E. Temperature-Dependent Response to C₃H₇OH and C₂H₅OH Vapors Induced by Deposition of Au Nanoparticles on SnO₂/NiO Hollow Sphere-Based Conductometric Sensors. *Sens. Actuators B Chem.* **2020**, *316*, 128041. [[CrossRef](#)]
64. Li, H.; Chu, S.; Ma, Q.; Li, H.; Che, Q.; Wang, J.; Wang, G.; Yang, P. Multilevel Effective Heterojunctions Based on SnO₂/ZnO 1D Fibrous Hierarchical Structure with Unique Interface Electronic Effects. *ACS Appl. Mater. Interfaces* **2019**, *11*, 31551–31561. [[CrossRef](#)]
65. Li, R.; Chen, S.; Lou, Z.; Li, L.; Huang, T.; Song, Y.; Chen, D.; Shen, G. Fabrication of Porous SnO₂ Nanowires Gas Sensors with Enhanced Sensitivity. *Sens. Actuators B Chem.* **2017**, *252*, 79–85. [[CrossRef](#)]
66. Reddy, C.S.; Murali, G.; Reddy, A.S.; Park, S.; In, I. GO Incorporated SnO₂ Nanotubes as Fast Response Sensors for Ethanol Vapor in Different Atmospheres. *J. Alloy. Compd.* **2020**, *813*, 152251. [[CrossRef](#)]
67. Mohanapriya, P.; Segawa, H.; Watanabe, K.; Watanabe, K.; Samitsu, S.; Natarajan, T.S.; Jaya, N.V.; Ohashi, N. Enhanced Ethanol-Gas Sensing Performance of Ce-Doped SnO₂ Hollow Nanofibers Prepared by Electrospinning. *Sens. Actuators B Chem.* **2013**, *188*, 872–878. [[CrossRef](#)]
68. Wang, T.T.; Ma, S.Y.; Cheng, L.; Luo, J.; Jiang, X.H.; Jin, W.X. Preparation of Yb-Doped SnO₂ Hollow Nanofibers with an Enhanced Ethanol-Gas Sensing Performance by Electrospinning. *Sens. Actuators B Chem.* **2015**, *216*, 212–220. [[CrossRef](#)]
69. Kida, T.; Suematsu, K.; Hara, K.; Kanie, K.; Muramatsu, A. Ultrasensitive Detection of Volatile Organic Compounds by a Pore Tuning Approach Using Anisotropically Shaped SnO₂ Nanocrystals. *ACS Appl. Mater. Interfaces* **2016**, *8*, 35485–35495. [[CrossRef](#)]
70. Ponzoni, A. Morphological Effects in SnO₂ Chemiresistors for Ethanol Detection: A Review in Terms of Central Performances and Outliers. *Sensors* **2021**, *21*, 29. [[CrossRef](#)]

71. Lee, S.-H.; Galstyan, V.; Ponzoni, A.; Gonzalo-Juan, I.; Riedel, R.; Dourges, M.-A.; Nicolas, Y.; Toupance, T. Finely Tuned SnO₂ Nanoparticles for Efficient Detection of Reducing and Oxidizing Gases: The Influence of Alkali Metal Cation on Gas-Sensing Properties. *ACS Appl. Mater. Interfaces* **2018**, *10*, 10173–10184. [[CrossRef](#)] [[PubMed](#)]
72. Lu, S.; Zhang, Y.; Liu, J.; Li, H.-Y.; Hu, Z.; Luo, X.; Gao, N.; Zhang, B.; Jiang, J.; Zhong, A.; et al. Sensitive H₂ Gas Sensors Based on SnO₂ Nanowires. *Sens. Actuators B Chem.* **2021**, *345*, 130334. [[CrossRef](#)]
73. Firooz, A.A.; Mahjoub, A.R.; Khodadadi, A.A. Highly Sensitive CO and Ethanol Nanoflower-like SnO₂ Sensor among Various Morphologies Obtained by Using Single and Mixed Ionic Surfactant Templates. *Sens. Actuators B Chem.* **2009**, *141*, 89–96. [[CrossRef](#)]
74. Ling-min, Y.; Sheng, L.; Bing, Y.; Miao-miao, H.; Meng-di, K.; Xinhui, F. A Highly Sensitive Ethanol Gas Sensor Based on Mesoporous SnO₂ Fabricated from a Facile Double-Surfactant Template Method. *Mater. Lett.* **2015**, *158*, 409–412. [[CrossRef](#)]
75. Yoon, J.-W.; Choi, S.H.; Kim, J.-S.; Jang, H.W.; Kang, Y.C.; Lee, J.-H. Trimodally Porous SnO₂ Nanospheres with Three-Dimensional Interconnectivity and Size Tunability: A One-Pot Synthetic Route and Potential Application as an Extremely Sensitive Ethanol Detector. *NPG Asia Mater.* **2016**, *8*, e244. [[CrossRef](#)]
76. Zhang, D.; Liu, Z.; Li, C.; Tang, T.; Liu, X.; Han, S.; Lei, B.; Zhou, C. Detection of NO₂ down to Ppb Levels Using Individual and Multiple In₂O₃ Nanowire Devices. *Nano Lett.* **2004**, *4*, 1919–1924. [[CrossRef](#)]
77. Wang, S.-H.; Chou, T.-C.; Liu, C.-C. Nano-Crystalline Tungsten Oxide NO₂ Sensor. *Sens. Actuators B Chem.* **2003**, *94*, 343–351. [[CrossRef](#)]
78. Oros, C.; Horprathum, M.; Wisitorsa, A.; Srichaiyaperk, T.; Samransuksamer, B.; Limwichean, S.; Eiamchai, P.; Phokharatkul, D.; Nuntawong, N.; Chananonawathorn, C.; et al. Ultra-Sensitive NO₂ Sensor Based on Vertically Aligned SnO₂ Nanorods Deposited by DC Reactive Magnetron Sputtering with Glancing Angle Deposition Technique. *Sens. Actuators B Chem.* **2016**, *223*, 936–945. [[CrossRef](#)]
79. Kida, T.; Nishiyama, A.; Hua, Z.; Suematsu, K.; Yuasa, M.; Shimano, K. WO₃ Nanolamella Gas Sensor: Porosity Control Using SnO₂ Nanoparticles for Enhanced NO₂ Sensing. *Langmuir* **2014**, *30*, 2571–2579. [[CrossRef](#)]
80. Ponzoni, A.; Comini, E.; Sberveglieri, G.; Zhou, J.; Deng, S.Z.; Xu, N.S.; Ding, Y.; Wang, Z.L. Ultrasensitive and Highly Selective Gas Sensors Using Three-Dimensional Tungsten Oxide Nanowire Networks. *Appl. Phys. Lett.* **2006**, *88*, 203101. [[CrossRef](#)]
81. Cai, Z.; Park, S. Enhancement Mechanisms of Ethanol-Sensing Properties Based on Cr₂O₃ Nanoparticle-Anchored SnO₂ Nanowires. *J. Mater. Res. Technol.* **2020**, *9*, 271–281. [[CrossRef](#)]
82. Park, J.Y.; Choi, S.-W.; Kim, S.S. Tailoring the Number of Junctions per Electrode Pair in Networked ZnO Nanowire Sensors. *J. Am. Ceram. Soc.* **2011**, *94*, 3922–3926. [[CrossRef](#)]
83. Li, T.; Zeng, W.; Zhao, W. Gas Sensing Performance of Multiple SnO₂ 1D Nanostructures Based on Their Interconnect Manner. *Mater. Lett.* **2016**, *167*, 230–233. [[CrossRef](#)]
84. Li, T.; Zeng, W. New Insight into the Gas Sensing Performance of SnO₂ Nanorod-Assembled Urchins Based on Their Assembly Density. *Ceram. Int.* **2017**, *43*, 728–735. [[CrossRef](#)]
85. Batzill, M.; Diebold, U. The Surface and Materials Science of Tin Oxide. *Prog. Surf. Sci.* **2005**, *79*, 47–154. [[CrossRef](#)]
86. Diebold, U. The Surface Science of Titanium Dioxide. *Surf. Sci. Rep.* **2003**, *48*, 53–229. [[CrossRef](#)]
87. Katsiev, K.; Kolmakov, A.; Fang, M.; Diebold, U. Characterization of Individual SnO₂ Nanobelts with STM. *Surf. Sci.* **2008**, *602*, L112–L114. [[CrossRef](#)]
88. Zhang, N.; Fan, Y.; Lu, Y.; Li, C.; Zhou, J.; Li, X.; Adimi, S.; Ruan, S. Synthesis of Au-Decorated SnO₂ Crystallites with Exposed (221) Facets and Their Enhanced Acetylene Sensing Properties. *Sens. Actuators B Chem.* **2020**, *307*, 127629. [[CrossRef](#)]
89. Chen, H.; Ma, S.Y.; Jin, W.X.; Li, W.Q. The Mode of Multi-Tier Nested Tin Dioxide Polyhedral Nanoparticles with Exposed High-Energy Facets and Their Gas Sensing Properties. *Mater. Lett.* **2016**, *164*, 627–630. [[CrossRef](#)]
90. Shang, Y.; Guo, L. Facet-Controlled Synthetic Strategy of Cu₂O-Based Crystals for Catalysis and Sensing. *Adv. Sci.* **2015**, *2*, 1500140. [[CrossRef](#)]
91. Han, X.; Jin, M.; Xie, S.; Kuang, Q.; Jiang, Z.; Jiang, Y.; Xie, Z.; Zheng, L. Synthesis of Tin Dioxide Octahedral Nanoparticles with Exposed High-Energy {221} Facets and Enhanced Gas-Sensing Properties. *Angew. Chem. Int. Ed.* **2009**, *48*, 9180–9183. [[CrossRef](#)]
92. Ouyang, J.; Pei, J.; Kuang, Q.; Xie, Z.; Zheng, L. Supersaturation-Controlled Shape Evolution of α-Fe₂O₃ Nanocrystals and Their Facet-Dependent Catalytic and Sensing Properties. *ACS Appl. Mater. Interfaces* **2014**, *6*, 12505–12514. [[CrossRef](#)]
93. Yang, Y.; Hong, A.; Liang, Y.; Xu, K.; Yu, T.; Shi, J.; Zeng, F.; Qu, Y.; Liu, Y.; Ding, M.; et al. High-Energy {001} Crystal Facets and Surface Fluorination Engineered Gas Sensing Properties of Anatase Titania Nanocrystals. *Appl. Surf. Sci.* **2017**, *423*, 602–610. [[CrossRef](#)]
94. Gao, X.; Zhang, T. An Overview: Facet-Dependent Metal Oxide Semiconductor Gas Sensors. *Sens. Actuators B Chem.* **2018**, *277*, 604–633. [[CrossRef](#)]
95. Ponzoni, A.; Baratto, C.; Bianchi, S.; Comini, E.; Ferroni, M.; Pardo, M.; Vezzoli, M.; Vomiero, A.; Faglia, G.; Sberveglieri, G. Metal Oxide Nanowire and Thin-Film-Based Gas Sensors for Chemical Warfare Simulants Detection. *IEEE Sens. J.* **2008**, *8*, 735–742. [[CrossRef](#)]
96. Sze, S.M.; Ng, K.K. Chapter 1 Physics and Properties of Semiconductors—A review. In *Physics of Semiconductor Devices*, 3rd ed.; John Wiley & Sons: Hoboken, NJ, USA, 2007; pp. 7–78. ISBN 978-0-471-14323-9.
97. Carotta, M.C.; Ferroni, M.; Guidi, V.; Martinelli, G. Preparation and Characterization of Nanostructured Titania Thick Films. *Adv. Mater.* **1999**, *11*, 943–946. [[CrossRef](#)]

98. Gribb, A.A.; Banfield, J.F. Particle Size Effects on Transformation Kinetics and Phase Stability in Nanocrystalline TiO₂. *Am. Mineral.* **1997**, *82*, 717–728. [[CrossRef](#)]
99. Ruiz, A.; Dezanneau, G.; Arbiol, J.; Cornet, A.; Morante, J.R. Study of the Influence of Nb Content and Sintering Temperature on TiO₂ Sensing Films. *Thin Solid Film.* **2003**, *436*, 90–94. [[CrossRef](#)]
100. Sysoev, V.V.; Schneider, T.; Goschnick, J.; Kiselev, I.; Habicht, W.; Hahn, H.; Strelcov, E.; Kolmakov, A. Percolating SnO₂ Nanowire Network as a Stable Gas Sensor: Direct Comparison of Long-Term Performance versus SnO₂ Nanoparticle Films. *Sens. Actuators B Chem.* **2009**, *139*, 699–703. [[CrossRef](#)]
101. Afzal, A. β -Ga₂O₃ Nanowires and Thin Films for Metal Oxide Semiconductor Gas Sensors: Sensing Mechanisms and Performance Enhancement Strategies. *J. Mater.* **2019**, *5*, 542–557. [[CrossRef](#)]
102. Fleischer, M.; Höllbauer, L.; Meixner, H. Effect of the Sensor Structure on the Stability of Ga₂O₃ Sensors for Reducing Gases. *Sens. Actuators B Chem.* **1994**, *18*, 119–124. [[CrossRef](#)]
103. Bae, M.-S.; Kim, S.-H.; Baek, J.-S.; Koh, J.-H. Comparative Study of High-Temperature Annealed and RTA Process β -Ga₂O₃ Thin Film by Sol–Gel Process. *Coatings* **2021**, *11*, 1220. [[CrossRef](#)]
104. Korotcenkov, G.; Brinzari, V.; Ivanov, M.; Cerneavski, A.; Rodriguez, J.; Cirera, A.; Cornet, A.; Morante, J. Structural Stability of Indium Oxide Films Deposited by Spray Pyrolysis during Thermal Annealing. *Thin Solid Film.* **2005**, *479*, 38–51. [[CrossRef](#)]
105. Cuong, N.D.; Park, Y.W.; Yoon, S.G. Microstructural and Electrical Properties of Ga₂O₃ Nanowires Grown at Various Temperatures by Vapor–Liquid–Solid Technique. *Sens. Actuators B Chem.* **2009**, *140*, 240–244. [[CrossRef](#)]
106. Krawczyk, M.; Suchorska-Woźniak, P.; Szukiewicz, R.; Kuchowicz, M.; Korbutowicz, R.; Teterycz, H. Morphology of Ga₂O₃ Nanowires and Their Sensitivity to Volatile Organic Compounds. *Nanomaterials* **2021**, *11*, 456. [[CrossRef](#)]
107. Ruiz, A.; Cornet, A.; Sakai, G.; Shimano, K.; Morante, J.R.; Yamazoe, N. Preparation of Cr-Doped TiO₂ Thin Film of P-Type Conduction for Gas Sensor Application. *Chem. Lett.* **2002**, *31*, 892–893. [[CrossRef](#)]
108. Kwak, C.-H.; Kim, T.-H.; Jeong, S.-Y.; Yoon, J.-W.; Kim, J.-S.; Lee, J.-H. Humidity-Independent Oxide Semiconductor Chemiresistors Using Terbium-Doped SnO₂ Yolk–Shell Spheres for Real-Time Breath Analysis. *ACS Appl. Mater. Interfaces* **2018**, *10*, 18886–18894. [[CrossRef](#)]
109. Hammer, C.; Warmer, J.; Maurer, S.; Kaul, P.; Thoelen, R.; Jung, N. A Compact 16 Channel Embedded System with High Dynamic Range Readout and Heater Management for Semiconducting Metal Oxide Gas Sensors. *Electronics* **2020**, *9*, 1855. [[CrossRef](#)]
110. Hijazi, Z.; Grassi, M.; Caviglia, D.D.; Valle, M. Time-Based Calibration-Less Read-out Circuit for Interfacing Wide Range MOX Gas Sensors. *Integration* **2018**, *63*, 232–239. [[CrossRef](#)]
111. Vakifahmetoglu, C.; Buldu, M.; Karakuscu, A.; Ponzoni, A.; Assefa, D.; Soraru, G.D. High Surface Area Carbonous Components from Emulsion Derived SiOC and Their Gas Sensing Behavior. *J. Eur. Ceram. Soc.* **2015**, *35*, 4447–4452. [[CrossRef](#)]
112. Bao, Y.; Wei, P.; Xia, X.; Huang, Z.; Homewood, K.; Gao, Y. Remarkably Enhanced H₂ Response and Detection Range in Nb Doped Rutile/Anatase Heterophase Junction TiO₂ Thin Film Hydrogen Sensors. *Sens. Actuators B Chem.* **2019**, *301*, 127143. [[CrossRef](#)]
113. Galstyan, V.; Ponzoni, A.; Kholmanov, I.; Natile, M.M.; Comini, E.; Nematov, S.; Sberveglieri, G. Investigation of Reduced Graphene Oxide and a Nb-Doped TiO₂ Nanotube Hybrid Structure To Improve the Gas-Sensing Response and Selectivity. *ACS Sens.* **2019**, *4*, 2094–2100. [[CrossRef](#)]
114. Goto, K.; Konishi, K.; Murakami, H.; Kumagai, Y.; Monemar, B.; Higashiwaki, M.; Kuramata, A.; Yamakoshi, S. Halide Vapor Phase Epitaxy of Si Doped β -Ga₂O₃ and Its Electrical Properties. *Thin Solid Film.* **2018**, *666*, 182–184. [[CrossRef](#)]
115. Mazeina, L.; Picard, Y.N.; Maximenko, S.I.; Perkins, F.K.; Glaser, E.R.; Twigg, M.E.; Freitas, J.A.; Prokes, S.M. Growth of Sn-Doped β -Ga₂O₃ Nanowires and Ga₂O₃–SnO₂ Heterostructures for Gas Sensing Applications. *Cryst. Growth Des.* **2009**, *9*, 4471–4479. [[CrossRef](#)]
116. Li, Y.; Trinch, A.; Wlodarski, W.; Galatsis, K.; Kalantar-zadeh, K. Investigation of the Oxygen Gas Sensing Performance of Ga₂O₃ Thin Films with Different Dopants. *Sens. Actuators B Chem.* **2003**, *93*, 431–434. [[CrossRef](#)]
117. Wang, D.; Lou, Y.; Wang, R.; Wang, P.; Zheng, X.; Zhang, Y.; Jiang, N. Humidity Sensor Based on Ga₂O₃ Nanorods Doped with Na⁺ and K⁺ from GaN Powder. *Ceram. Int.* **2015**, *41*, 14790–14797. [[CrossRef](#)]
118. Singh, N.; Ponzoni, A.; Comini, E.; Lee, P.S. Chemical Sensing Investigations on Zn–In₂O₃ Nanowires. *Sens. Actuators B Chem.* **2012**, *171*, 244–248. [[CrossRef](#)]
119. Sun, X.; Liu, X.; Deng, X.; Xu, X. Synthesis of Zn-Doped In₂O₃ Nano Sphere Architectures as a Triethylamine Gas Sensor and Photocatalytic Properties. *RSC Adv.* **2016**, *6*, 89847–89854. [[CrossRef](#)]
120. Li, P.; Fan, H.; Cai, Y.; Xu, M.; Long, C.; Li, M.; Lei, S.; Zou, X. Phase Transformation (Cubic to Rhombohedral): The Effect on the NO₂ Sensing Performance of Zn-Doped Flower-like In₂O₃ Structures. *RSC Adv.* **2014**, *4*, 15161–15170. [[CrossRef](#)]
121. Zhao, Q.; Ju, D.; Deng, X.; Huang, J.; Cao, B.; Xu, X. Morphology-Modulation of SnO₂ Hierarchical Architectures by Zn Doping for Glycol Gas Sensing and Photocatalytic Applications. *Sci. Rep.* **2015**, *5*, 7874. [[CrossRef](#)]
122. Rumyantseva, M.N.; Safonova, O.V.; Boulova, M.N.; Ryabova, L.I.; Gas'kov, A.M. Dopants in Nanocrystalline Tin Dioxide. *Russ. Chem. Bull.* **2003**, *52*, 1217–1238. [[CrossRef](#)]
123. Degler, D.; Weimar, U.; Barsan, N. Current Understanding of the Fundamental Mechanisms of Doped and Loaded Semiconducting Metal-Oxide-Based Gas Sensing Materials. *ACS Sens.* **2019**, *4*, 2228–2249. [[CrossRef](#)] [[PubMed](#)]
124. Walker, J.M.; Akbar, S.A.; Morris, P.A. Synergistic Effects in Gas Sensing Semiconducting Oxide Nano-Heterostructures: A Review. *Sens. Actuators B Chem.* **2019**, *286*, 624–640. [[CrossRef](#)]

125. Lin, T.; Lv, X.; Li, S.; Wang, Q. The Morphologies of the Semiconductor Oxides and Their Gas-Sensing Properties. *Sensors* **2017**, *17*, 2779. [[CrossRef](#)] [[PubMed](#)]
126. Sze, S.M.; Ng, K.K. Chapter 3 Metal-Semiconductors Contacts. In *Physics of Semiconductor Devices*, 3rd ed.; John Wiley & Sons: Hoboken NJ, USA, 2007; pp. 134–196. ISBN 978-0-471-14323-9.
127. Roldán, A.; González, S.; Ricart, J.M.; Illas, F. Critical Size for O₂ Dissociation by Au Nanoparticles. *ChemPhysChem* **2009**, *10*, 348–351. [[CrossRef](#)]
128. Tofighi, G.; Degler, D.; Junker, B.; Müller, S.; Lichtenberg, H.; Wang, W.; Weimar, U.; Barsan, N.; Grunwaldt, J.-D. Microfluidically Synthesized Au, Pd and AuPd Nanoparticles Supported on SnO₂ for Gas Sensing Applications. *Sens. Actuators B Chem.* **2019**, *292*, 48–56. [[CrossRef](#)]
129. Kolmakov, A.; Klenov, D.O.; Lilach, Y.; Stemmer, S.; Moskovits, M. Enhanced Gas Sensing by Individual SnO₂ Nanowires and Nanobelts Functionalized with Pd Catalyst Particles. *Nano Lett.* **2005**, *5*, 667–673. [[CrossRef](#)]
130. Li, Y.; Zhao, F.-X.; Lian, X.-X.; Zou, Y.-L.; Wang, Q.; Zhou, Q.-J. Highly Sensitive Ethanol Sensor Based on Au-Decorated SnO₂ Nanoparticles Synthesized Through Precipitation and Microwave Irradiation. *J. Electron. Mater.* **2016**, *45*, 3149–3156. [[CrossRef](#)]
131. Jin, C.; Kim, H.; Park, S.; Kim, H.W.; Lee, S.; Lee, C. Enhanced Ethanol Gas Sensing Properties of SnO₂ Nanobelts Functionalized with Au. *Ceram. Int.* **2012**, *38*, 6585–6590. [[CrossRef](#)]
132. Kim, B.-Y.; Cho, J.S.; Yoon, J.-W.; Na, C.W.; Lee, C.-S.; Ahn, J.H.; Kang, Y.C.; Lee, J.-H. Extremely Sensitive Ethanol Sensor Using Pt-Doped SnO₂ Hollow Nanospheres Prepared by Kirkendall Diffusion. *Sens. Actuators B Chem.* **2016**, *234*, 353–360. [[CrossRef](#)]
133. Xue, X.; Chen, Z.; Ma, C.; Xing, L.; Chen, Y.; Wang, Y.; Wang, T. One-Step Synthesis and Gas-Sensing Characteristics of Uniformly Loaded Pt@SnO₂ Nanorods. *J. Phys. Chem. C* **2010**, *114*, 3968–3972. [[CrossRef](#)]
134. Punginsang, M.; Zappa, D.; Comini, E.; Wisitsoraat, A.; Sberveglieri, G.; Ponzoni, A.; Liewhiran, C. Selective H₂S Gas Sensors Based on Ohmic Hetero-Interface of Au-Functionalized WO₃ Nanowires. *Appl. Surf. Sci.* **2022**, *571*, 151262. [[CrossRef](#)]
135. Lee, I.; Choi, S.-J.; Park, K.-M.; Lee, S.S.; Choi, S.; Kim, I.-D.; Park, C.O. The Stability, Sensitivity and Response Transients of ZnO, SnO₂ and WO₃ Sensors under Acetone, Toluene and H₂S Environments. *Sens. Actuators B Chem.* **2014**, *197*, 300–307. [[CrossRef](#)]
136. Krivetskiy, V.; Zamanskiy, K.; Beltyukov, A.; Asachenko, A.; Topchiy, M.; Nechaev, M.; Garshev, A.; Krotova, A.; Filatova, D.; Maslakov, K.; et al. Effect of AuPd Bimetal Sensitization on Gas Sensing Performance of Nanocrystalline SnO₂ Obtained by Single Step Flame Spray Pyrolysis. *Nanomaterials* **2019**, *9*, 728. [[CrossRef](#)]
137. Li, G.; Cheng, Z.; Xiang, Q.; Yan, L.; Wang, X.; Xu, J. Bimetal PdAu Decorated SnO₂ Nanosheets Based Gas Sensor with Temperature-Dependent Dual Selectivity for Detecting Formaldehyde and Acetone. *Sens. Actuators B Chem.* **2019**, *283*, 590–601. [[CrossRef](#)]
138. Zeb, S.; Peng, X.; Shi, Y.; Su, J.; Sun, J.; Zhang, M.; Sun, G.; Nie, Y.; Cui, Y.; Jiang, X. Bimetal Au-Pd Decorated Hierarchical WO₃ Nanowire Bundles for Gas Sensing Application. *Sens. Actuators B Chem.* **2021**, *334*, 129584. [[CrossRef](#)]
139. Wei, T.-Y.; Yeh, P.-H.; Lu, S.-Y.; Wang, Z.L. Gigantic Enhancement in Sensitivity Using Schottky Contacted Nanowire Nanosensor. *J. Am. Chem. Soc.* **2009**, *131*, 17690–17695. [[CrossRef](#)]
140. Navale, S.; Shahbaz, M.; Majhi, S.M.; Mirzaei, A.; Kim, H.W.; Kim, S.S. Cu₂O Nanostructure-Based Gas Sensors for H₂S Detection: An Overview. *Chemosensors* **2021**, *9*, 127. [[CrossRef](#)]
141. Shao, F.; Hoffmann, M.W.G.; Prades, J.D.; Zamani, R.; Arbiol, J.; Morante, J.R.; Varechkina, E.; Rumyantseva, M.; Gaskov, A.; Giebelhaus, I.; et al. Heterostructured P-CuO (Nanoparticle)/n-SnO₂ (Nanowire) Devices for Selective H₂S Detection. *Sens. Actuators B Chem.* **2013**, *181*, 130–135. [[CrossRef](#)]
142. Wang, T.; Zhang, S.; Yu, Q.; Wang, S.; Sun, P.; Lu, H.; Liu, F.; Yan, X.; Lu, G. Novel Self-Assembly Route Assisted Ultra-Fast Trace Volatile Organic Compounds Gas Sensing Based on Three-Dimensional Opal Microspheres Composites for Diabetes Diagnosis. *ACS Appl. Mater. Interfaces* **2018**, *10*, 32913–32921. [[CrossRef](#)]
143. Zhao, S.; Shen, Y.; Maboudian, R.; Carraro, C.; Han, C.; Liu, W.; Wei, D. Facile Synthesis of ZnO-SnO₂ Hetero-Structured Nanowires for High-Performance NO₂ Sensing Application. *Sens. Actuators B Chem.* **2021**, *333*, 129613. [[CrossRef](#)]
144. Choi, S.-B.; Lee, W.S.; Lee, C.; Lee, S. Enhanced NO₂ Gas-Sensing Performance of Pd/ZnO-Codecorated SnO₂ Nanorod Sensors. *Appl. Phys. A* **2018**, *124*, 817. [[CrossRef](#)]
145. Kim, J.-H.; Katoch, A.; Kim, S.S. Optimum Shell Thickness and Underlying Sensing Mechanism in p-n CuO-ZnO Core-Shell Nanowires. *Sens. Actuators B Chem.* **2016**, *222*, 249–256. [[CrossRef](#)]
146. Kim, J.-H.; Katoch, A.; Kim, S.-H.; Kim, S.S. Chemiresistive Sensing Behavior of SnO₂ (n)-Cu₂O (p) Core-Shell Nanowires. *ACS Appl. Mater. Interfaces* **2015**, *7*, 15351–15358. [[CrossRef](#)] [[PubMed](#)]
147. Choi, S.-W.; Katoch, A.; Sun, G.-J.; Kim, J.-H.; Kim, S.-H.; Kim, S.S. Dual Functional Sensing Mechanism in SnO₂-ZnO Core-Shell Nanowires. *ACS Appl. Mater. Interfaces* **2014**, *6*, 8281–8287. [[CrossRef](#)] [[PubMed](#)]
148. Tharsika, T.; Haseeb, A.S.M.A.; Akbar, S.A.; Sabri, M.F.; Hoong, W.Y. Enhanced Ethanol Gas Sensing Properties of SnO₂-Core/ZnO-Shell Nanostructures. *Sensors* **2014**, *14*, 14586–14600. [[CrossRef](#)] [[PubMed](#)]
149. Ju, D.-X.; Xu, H.-Y.; Qiu, Z.-W.; Zhang, Z.-C.; Xu, Q.; Zhang, J.; Wang, J.-Q.; Cao, B.-Q. Near Room Temperature, Fast-Response, and Highly Sensitive Triethylamine Sensor Assembled with Au-Loaded ZnO/SnO₂ Core-Shell Nanorods on Flat Alumina Substrates. *ACS Appl. Mater. Interfaces* **2015**, *7*, 19163–19171. [[CrossRef](#)]
150. Jang, Y.-G.; Kim, W.-S.; Kim, D.-H.; Hong, S.-H. Fabrication of Ga₂O₃/SnO₂ Core-Shell Nanowires and Their Ethanol Gas Sensing Properties. *J. Mater. Res.* **2011**, *26*, 2322–2327. [[CrossRef](#)]

151. Xue, X.-T.; Zhu, L.-Y.; Yuan, K.-P.; Zeng, C.; Li, X.-X.; Ma, H.-P.; Lu, H.-L.; Zhang, D.W. ZnO Branched P-CuxO @n-ZnO Heterojunction Nanowires for Improving Acetone Gas Sensing Performance. *Sens. Actuators B Chem.* **2020**, *324*, 128729. [[CrossRef](#)]
152. Bang, J.H.; Mirzaei, A.; Han, S.; Lee, H.Y.; Shin, K.Y.; Kim, S.S.; Kim, H.W. Realization of Low-Temperature and Selective NO₂ Sensing of SnO₂ Nanowires via Synergistic Effects of Pt Decoration and Bi₂O₃ Branching. *Ceram. Int.* **2021**, *47*, 5099–5111. [[CrossRef](#)]
153. Choi, M.S.; Bang, J.H.; Mirzaei, A.; Oum, W.; Na, H.G.; Jin, C.; Kim, S.S.; Kim, H.W. Promotional Effects of ZnO-Branching and Au-Functionalization on the Surface of SnO₂ Nanowires for NO₂ Sensing. *J. Alloy. Compd.* **2019**, *786*, 27–39. [[CrossRef](#)]
154. Kwon, Y.J.; Kang, S.Y.; Mirzaei, A.; Choi, M.S.; Bang, J.H.; Kim, S.S.; Kim, H.W. Enhancement of Gas Sensing Properties by the Functionalization of ZnO-Branched SnO₂ Nanowires with Cr₂O₃ Nanoparticles. *Sens. Actuators B Chem.* **2017**, *249*, 656–666. [[CrossRef](#)]
155. Wan, Q.; Huang, J.; Xie, Z.; Wang, T.; Dattoli, E.N.; Lu, W. Branched SnO₂ Nanowires on Metallic Nanowire Backbones for Ethanol Sensors Application. *Appl. Phys. Lett.* **2008**, *92*, 102101. [[CrossRef](#)]
156. Li, X.; Tao, L.; Chen, Z.; Fang, H.; Li, X.; Wang, X.; Xu, J.-B.; Zhu, H. Graphene and Related Two-Dimensional Materials: Structure-Property Relationships for Electronics and Optoelectronics. *Appl. Phys. Rev.* **2017**, *4*, 021306. [[CrossRef](#)]
157. Schedin, F.; Geim, A.K.; Morozov, S.V.; Hill, E.W.; Blake, P.; Katsnelson, M.I.; Novoselov, K.S. Detection of Individual Gas Molecules Adsorbed on Graphene. *Nat. Mater.* **2007**, *6*, 652–655. [[CrossRef](#)]
158. Robinson, J.T.; Perkins, F.K.; Snow, E.S.; Wei, Z.; Sheehan, P.E. Reduced Graphene Oxide Molecular Sensors. *Nano Lett.* **2008**, *8*, 3137–3140. [[CrossRef](#)]
159. Xia, Y.; Wang, J.; Xu, J.-L.; Li, X.; Xie, D.; Xiang, L.; Komarneni, S. Confined Formation of Ultrathin ZnO Nanorods/Reduced Graphene Oxide Mesoporous Nanocomposites for High-Performance Room-Temperature NO₂ Sensors. *ACS Appl. Mater. Interfaces* **2016**, *8*, 35454–35463. [[CrossRef](#)]
160. Liu, Z.; Yu, L.; Guo, F.; Liu, S.; Qi, L.; Shan, M.; Fan, X. Facial Development of High Performance Room Temperature NO₂ Gas Sensors Based on ZnO Nanowalls Decorated RGO Nanosheets. *Appl. Surf. Sci.* **2017**, *423*, 721–727. [[CrossRef](#)]
161. Cao, P.; Cai, Y.; Pawar, D.; Navale, S.T.; Rao, C.N.; Han, S.; Xu, W.; Fang, M.; Liu, X.; Zeng, Y.; et al. Down to Ppb Level NO₂ Detection by ZnO/RGO Heterojunction Based Chemiresistive Sensors. *Chem. Eng. J.* **2020**, *401*, 125491. [[CrossRef](#)]
162. Sun, Z.; Huang, D.; Yang, Z.; Li, X.; Hu, N.; Yang, C.; Wei, H.; Yin, G.; He, D.; Zhang, Y. ZnO Nanowire-Reduced Graphene Oxide Hybrid Based Portable NH₃ Gas Sensing Electron Device. *IEEE Electron Device Lett.* **2015**, *36*, 1376–1379. [[CrossRef](#)]
163. Chen, Z.; Guo, H.; Zhang, F.; Li, X.; Yu, J.; Chen, X. Porous ZnO/RGO Nanosheet-Based NO₂ Gas Sensor with High Sensitivity and Ppb-Level Detection Limit at Room Temperature. *Adv. Mater. Interfaces* **2021**, *8*, 2101511. [[CrossRef](#)]
164. Feng, Q.; Li, X.; Wang, J. Percolation Effect of Reduced Graphene Oxide (RGO) on Ammonia Sensing of RGO-SnO₂ Composite Based Sensor. *Sens. Actuators B Chem.* **2017**, *243*, 1115–1126. [[CrossRef](#)]
165. Song, Z.; Wei, Z.; Wang, B.; Luo, Z.; Xu, S.; Zhang, W.; Yu, H.; Li, M.; Huang, Z.; Zang, J.; et al. Sensitive Room-Temperature H₂S Gas Sensors Employing SnO₂ Quantum Wire/Reduced Graphene Oxide Nanocomposites. *Chem. Mater.* **2016**, *28*, 1205–1212. [[CrossRef](#)]
166. Shewale, P.S.; Yun, K.-S. Synthesis and Characterization of Cu-Doped ZnO/RGO Nanocomposites for Room-Temperature H₂S Gas Sensor. *J. Alloy. Compd.* **2020**, *837*, 155527. [[CrossRef](#)]
167. Fang, W.; Yang, Y.; Yu, H.; Dong, X.; Wang, R.; Wang, T.; Wang, J.; Liu, Z.; Zhao, B.; Wang, X. An In₂O₃ Nanorod-Decorated Reduced Graphene Oxide Composite as a High-Response NO_x Gas Sensor at Room Temperature. *New J. Chem.* **2017**, *41*, 7517–7523. [[CrossRef](#)]
168. Deng, S.; Tjoa, V.; Fan, H.M.; Tan, H.R.; Sayle, D.C.; Olivo, M.; Mhaisalkar, S.; Wei, J.; Sow, C.H. Reduced Graphene Oxide Conjugated Cu₂O Nanowire Mesocrystals for High-Performance NO₂ Gas Sensor. *J. Am. Chem. Soc.* **2012**, *134*, 4905–4917. [[CrossRef](#)] [[PubMed](#)]
169. Kampara, R.K.; Rai, P.K.; Jeyaprakash, B.G. Highly Sensitive Graphene Oxide Functionalized ZnO Nanowires for Ammonia Vapour Detection at Ambient Temperature. *Sens. Actuators B Chem.* **2018**, *255*, 1064–1071. [[CrossRef](#)]
170. Van Quang, V.; Van Dung, N.; Sy Trong, N.; Duc Hoa, N.; Van Duy, N.; Van Hieu, N. Outstanding Gas-Sensing Performance of Graphene/SnO₂ Nanowire Schottky Junctions. *Appl. Phys. Lett.* **2014**, *105*, 013107. [[CrossRef](#)]
171. Tyagi, P.; Sharma, A.; Tomar, M.; Gupta, V. A Comparative Study of RGO-SnO₂ and MWCNT-SnO₂ Nanocomposites Based SO₂ Gas Sensors. *Sens. Actuators B Chem.* **2017**, *248*, 980–986. [[CrossRef](#)]
172. Robinson, J.A.; Snow, E.S.; Bădescu, Ș.C.; Reinecke, T.L.; Perkins, F.K. Role of Defects in Single-Walled Carbon Nanotube Chemical Sensors. *Nano Lett.* **2006**, *6*, 1747–1751. [[CrossRef](#)] [[PubMed](#)]
173. Hou, P.-X.; Liu, C.; Cheng, H.-M. Purification of Carbon Nanotubes. *Carbon* **2008**, *46*, 2003–2025. [[CrossRef](#)]
174. Waclawik, E.R.; Chang, J.; Ponzoni, A.; Concina, I.; Zappa, D.; Comini, E.; Motta, N.; Faglia, G.; Sberveglieri, G. Functionalised Zinc Oxide Nanowire Gas Sensors: Enhanced NO₂ Gas Sensor Response by Chemical Modification of Nanowire Surfaces. *Beilstein J. Nanotechnol.* **2012**, *3*, 368–377. [[CrossRef](#)]
175. Singh, M.; Kaur, N.; Drera, G.; Casotto, A.; Sangaletti, L.; Comini, E. SAM Functionalized ZnO Nanowires for Selective Acetone Detection: Optimized Surface Specific Interaction Using APTMS and GLYMO Monolayers. *Adv. Funct. Mater.* **2020**, *30*, 2003217. [[CrossRef](#)]

176. Hoffmann, M.W.G.; Prades, J.D.; Mayrhofer, L.; Hernandez-Ramirez, F.; Järvi, T.T.; Moseler, M.; Waag, A.; Shen, H. Highly Selective SAM–Nanowire Hybrid NO₂ Sensor: Insight into Charge Transfer Dynamics and Alignment of Frontier Molecular Orbitals. *Adv. Funct. Mater.* **2014**, *24*, 595–602. [[CrossRef](#)]
177. Paolesse, R.; Nardis, S.; Monti, D.; Stefanelli, M.; Di Natale, C. Porphyrinoids for Chemical Sensor Applications. *Chem. Rev.* **2017**, *117*, 2517–2583. [[CrossRef](#)]
178. Magna, G.; Catini, A.; Kumar, R.; Palmacci, M.; Martinelli, E.; Paolesse, R.; Di Natale, C. Conductive Photo-Activated Porphyrin-ZnO Nanostructured Gas Sensor Array. *Sensors* **2017**, *17*, 747. [[CrossRef](#)]
179. Sivalingam, Y.; Martinelli, E.; Catini, A.; Magna, G.; Pomarico, G.; Basoli, F.; Paolesse, R.; Di Natale, C. Gas-Sensitive Photoconductivity of Porphyrin-Functionalized ZnO Nanorods. *J. Phys. Chem. C* **2012**, *116*, 9151–9157. [[CrossRef](#)]
180. Magna, G.; Muduganti, M.; Stefanelli, M.; Sivalingam, Y.; Zurlo, F.; Di Bartolomeo, E.; Catini, A.; Martinelli, E.; Paolesse, R.; Di Natale, C. Light-Activated Porphyrinoid-Capped Nanoparticles for Gas Sensing. *ACS Appl. Nano Mater.* **2021**, *4*, 414–424. [[CrossRef](#)]
181. Salehi, A. A Highly Sensitive Self Heated SnO₂ Carbon Monoxide Sensor. *Sens. Actuators B Chem.* **2003**, *96*, 88–93. [[CrossRef](#)]
182. Majhi, S.M.; Mirzaei, A.; Kim, H.W.; Kim, S.S.; Kim, T.W. Recent Advances in Energy-Saving Chemiresistive Gas Sensors: A Review. *Nano Energy* **2021**, *79*, 105369. [[CrossRef](#)]
183. Meng, G.; Zhuge, F.; Nagashima, K.; Nakao, A.; Kanai, M.; He, Y.; Boudot, M.; Takahashi, T.; Uchida, K.; Yanagida, T. Nanoscale Thermal Management of Single SnO₂ Nanowire: Pico-Joule Energy Consumed Molecule Sensor. *ACS Sens.* **2016**, *1*, 997–1002. [[CrossRef](#)]
184. Liu, H.; Zhang, L.; Li, K.H.; Tan, O.K. Microhotplates for Metal Oxide Semiconductor Gas Sensor Applications—Towards the CMOS-MEMS Monolithic Approach. *Micromachines* **2018**, *9*, 557. [[CrossRef](#)]
185. Lahlalia, A.; Le Neel, O.; Shankar, R.; Selberherr, S.; Filipovic, L. Improved Sensing Capability of Integrated Semiconducting Metal Oxide Gas Sensor Devices. *Sensors* **2019**, *19*, 374. [[CrossRef](#)]
186. Prades, J.D.; Jimenez-Diaz, R.; Hernandez-Ramirez, F.; Cirera, A.; Romano-Rodriguez, A.; Morante, J.R. Harnessing Self-Heating in Nanowires for Energy Efficient, Fully Autonomous and Ultra-Fast Gas Sensors. *Sens. Actuators B Chem.* **2010**, *144*, 1–5. [[CrossRef](#)]
187. Ngoc, T.M.; Van Duy, N.; Hung, C.M.; Hoa, N.D.; Trung, N.N.; Nguyen, H.; Van Hieu, N. Ultralow Power Consumption Gas Sensor Based on a Self-Heated Nanojunction of SnO₂ Nanowires. *RSC Adv.* **2018**, *8*, 36323–36330. [[CrossRef](#)]
188. Kim, J.-H.; Kim, H.W.; Kim, S.S. Self-Heating Effects on the Toluene Sensing of Pt-Functionalized SnO₂–ZnO Core–Shell Nanowires. *Sens. Actuators B Chem.* **2017**, *251*, 781–794. [[CrossRef](#)]
189. Fàbrega, C.; Casals, O.; Hernández-Ramírez, F.; Prades, J.D. A Review on Efficient Self-Heating in Nanowire Sensors: Prospects for Very-Low Power Devices. *Sens. Actuators B Chem.* **2018**, *256*, 797–811. [[CrossRef](#)]
190. Kunt, T.A.; McAvoy, T.J.; Cavicchi, R.E.; Semancik, S. Optimization of Temperature Programmed Sensing for Gas Identification Using Micro-Hotplate Sensors. *Sens. Actuators B Chem.* **1998**, *53*, 24–43. [[CrossRef](#)]
191. Meier, D.C.; Evju, J.K.; Boger, Z.; Raman, B.; Benkstein, K.D.; Martinez, C.J.; Montgomery, C.B.; Semancik, S. The Potential for and Challenges of Detecting Chemical Hazards with Temperature-Programmed Microsensors. *Sens. Actuators B Chem.* **2007**, *121*, 282–294. [[CrossRef](#)]
192. Krivetskiy, V.; Efitov, A.; Arkhipenko, A.; Vladimirova, S.; Rummyantseva, M.; Dolenko, S.; Gaskov, A. Selective Detection of Individual Gases and CO/H₂ Mixture at Low Concentrations in Air by Single Semiconductor Metal Oxide Sensors Working in Dynamic Temperature Mode. *Sens. Actuators B Chem.* **2018**, *254*, 502–513. [[CrossRef](#)]
193. Lee, A.P.; Reedy, B.J. Temperature Modulation in Semiconductor Gas Sensing. *Sens. Actuators B Chem.* **1999**, *60*, 35–42. [[CrossRef](#)]
194. Prades, J.D.; Hernández-Ramírez, F.; Fischer, T.; Hoffmann, M.; Müller, R.; López, N.; Mathur, S.; Morante, J.R. Quantitative Analysis of CO-Humidity Gas Mixtures with Self-Heated Nanowires Operated in Pulsed Mode. *Appl. Phys. Lett.* **2010**, *97*, 243105. [[CrossRef](#)]